American Mineralogist
Date: 6/10/2020

Subject: Manuscript-Revision 1 (No. #7508R)

# Fluid source and metal precipitation mechanism of sediment-hosted Chang'an orogenic gold deposit, SW China: constraints from sulfide texture, trace element, S, Pb and He–Ar isotopes and calcite C–O isotopes

Lin Yang [1], Qingfei Wang [1, *], Ross R. Large [2], Indrani Mukherjee [2], Jun Deng [1], Huajian Li [1], Huazhi Yu [1], Xuan Wang [1]

[1] State Key Laboratory of Geological Processes and Mineral Resources, China University of Geosciences, Beijing 100083, China

[2] Centre for Ore Deposit and Earth Sciences (CODES), University of Tasmania, Private Bag 126, Hobart, Tasmania 7001, Australia

* Author to whom correspondence should be addressed

Qingfei Wang: wqf@cugb.edu.cn

## Abstract

The source of fluids and mechanism of metal precipitation in sediment-hosted, disseminated orogenic gold deposits are ambiguous. Pyrite texture, trace element, S, Pb and He–Ar isotope compositions of sulfides and C–O isotope data of calcite from Chang'an orogenic gold deposit in the Ailaoshan orogenic belt, SW China, were studied to provide a new genetic model for the sediment-hosted orogenic gold deposit, and furthering knowledge of the source of fluids and their mechanism of metal precipitation. Orebodies at Chang'an are mainly hosted by Ordovician turbidite with minor in Oligocene syenite. Two stages of mineralization have been identified in the deposit: stage I disseminated quartz–arsenopyrite–pyrite, and stage II veined quartz–calcite–polymetallic sulfides. Five generations of pyrite have been identified in turbidite: pre-ore syn-sedimentary pyrite, $py_{I-1}$ and $py_{I-2}$ in stage I, and $py_{II-1}$ and $py_{II-2}$ in stage II, and an unzoned pyrite population developed in syenite. $Py_{I-1}$ commonly overgrows syn-sedimentary pyrite with irregular boundaries and contains arsenopyrite, galena, chalcopyrite and electrum inclusions along the boundaries. $Py_{I-1}$ is overgrown by thin and inclusion-free $py_{I-2}$, and crosscut by $py_{II-1}$, which is rimmed by $py_{II-2}$.

The syn-sedimentary pyrite is distributed parallel to the sedimentary bedding and contains As (620.8 ppm), Pb (61.6 ppm), Ni (59.8 ppm), Mo (54.4 ppm), Co (23.4 ppm), and Cu (13.0 ppm) with low Au content of 0.06 ppm. This pyrite has $\delta^{34}S$ values of –18.1 to +30.4 ‰ and high radiogenic Pb isotope ratios (average $^{206}Pb/^{204}Pb$, $^{207}Pb/^{204}Pb$ and $^{208}Pb/^{204}Pb$ of 19.05, 15.86 and 39.87, respectively). $Py_{I-1}$ and coexisting arsenopyrite are enriched in invisible Au (up to 227.1 ppm and 353.3 ppm, respectively),

As, Ni, Cu and Pb, while $py_{I-2}$ contain much lower trace element abundances relative to $py_{I-1}$ and arsenopyrite. Partial replacement of syn-sedimentary pyrite by $py_{I-1}$ plus arsenopyrite, galena, chalcopyrite and electrum, and similar Pb isotope ratios between syn-sedimentary pyrite and $py_{I-1}$ indicate that reaction of external deep Au-rich fluids with syn-sedimentary pyrite is responsible for gold precipitation in stage I. $Py_{I-1}$, arsenopyrite and $py_{I-2}$ show a narrower $\delta^{34}S$ range of –3.2 to 7.1 ‰ relative to syn-sedimentary pyrite, demonstrating that the fluid-pyrite interaction has homogenized the sulfur. The unzoned pyrite in syenite has similar mineral inclusions (arsenopyrite, galena, etc.), $\delta^{34}S$ values (+0.6 to 6.3 ‰) and Pb isotope ratios to $py_{I-1}$, but much lower trace element abundances relative to $py_{I-1}$. It may be attributed to different reactions of similar fluids with different wall-rocks. $Py_{II-1}$ and $py_{II-2}$ in stage II contain elevated As, Pb, Cu, Sb, Zn and Ag with low mean Au content (3.3 ppm) and have $\delta^{34}S$ ranges of –2.8 to +1.2 ‰ and –6.2 and –0.8 ‰, respectively. Galena in stage II has lower radiogenic Pb isotope ratios than stage I pyrites, indicative of a different Pb source or fluid evolution. The gases released from mixture of $py_{II-1}$-$py_{II-2}$ have R/Ra of 0.38 to 0.98 and $^{40}Ar^*/^4He$ of 0.50 to 1.34, falling between the fields of mantle-derived and crustal fluids. Late ore calcites have $\delta^{13}C_{PDB}$ of –8.7 to 2.7 ‰ and $\delta^{18}O_{PDB}$ of 8.05 to 25.58 ‰, also plotting between sedimentary carbonate and mantle fields. These signatures indicate that ore fluids in stage II are base metal-rich fluids with a small amount contribution from mantle. Different ore assemblages, trace element composition and isotope data between stages I and II at Chang'an suggest that the deposit experienced an evolution from early Au-rich fluids to late base metal-rich ones.

69 This study highlights that ore metals in sediment-hosted disseminated orogenic gold
70 deposits may be sourced from both deep fluids and local wall-rock, and that fluid-rock
71 interaction behaved as key control on ore precipitation.

72

73 Keywords: Pyrite texture, trace element, *in situ* S–Pb isotopes, sediment-hosted gold
74 deposit, Chang'an, Ailaoshan

75

## Introduction

(Meta)sediment-hosted, disseminated orogenic gold deposits are characterized by wide alteration zones and thick orebodies with low grade but commonly large tonnage (Wilde et al. 2001; Large et al. 2007, 2011; Steadman and Large 2016). Their ore precipitation mechanism and the source of metals, critical subjects for understanding ore-forming process and developing enhanced exploration strategies (Barker et al. 2009; Peterson and Mavrogenes 2014; Velasquez et al. 2014; Tanner et al. 2016; Voute et al. 2019), are poorly understood, thus attracting broad interest. Ore precipitation mechanisms for these orogenic gold deposits are diverse, and include flash boiling of fluids triggered by earthquake-induced fault-valve processes (Sibson and Scott 1998; Weatherley and Henley 2013), fluid-rock reaction (Evans et al. 2006; Li et al. 2019a), and fluid mixing (Bateman and Hagemann 2004). Moreover, the origin for the gold in these orogenic gold deposits has been hotly debated by two contrasting perspectives: locally sourced from metamorphic devolatilization reactions of sedimentary rocks (Large et al. 2007, 2009, 2011; Thomas et al. 2011) and deeply sourced reservoirs, including magmatic (Lawrence et al. 2013; Treloar et al. 2015), mantle (Graupner et al. 2006; Deng et al. 2019a, 2020; Wang et al. 2019), and metamorphic fluids (Pitcairn et al. 2006; Tomkins 2010; Lawrence et al. 2013; Chinnasamy et al. 2015).

Pyrite is the most common ore mineral that forms in different stages of fluid evolution during gold mineralization (e.g., Large et al. 2007; Deditius et al. 2014), which thus allows pyrite composition associated with Au and other metals to be traced by *in situ* microanalytical techniques throughout the history of formation of a deposit

98 (e.g., Large et al. 2007, 2009). Pyrite texture, paragenesis and trace element data have
99 been successfully interpreted to evaluate fluid composition and mechanisms of
100 incorporation or release of Au and other trace metals in different types of gold deposits
101 (Large et al. 2007, 2009, 2011; Thomas et al. 2011; Cook et al. 2013; Steadman and
102 Large 2016; Yang et al. 2016; Li et al. 2019a). Sulfur and lead isotopes in sulfide have
103 been used to determine the fluid source(s), interaction with wall-rocks (including earlier
104 generation of minerals), and fluid mixing processes (Ohmoto and Rye 1979; Chang et
105 al. 2008; Meffre et al. 2008; Woodhead et al. 2009). Noble gases may constrain the
106 fluid source because of their relatively unreactive nature, transportation with the major
107 volatiles, and element and isotope ratios that vary by orders of magnitude between
108 different reservoirs (e.g., Burnard et al. 1999; Mao et al. 2003; Graupner et al. 2006; Li
109 et al. 2010; Goodwin et al. 2017). Synthesizing the methods noted above is an effective
110 approach to understanding ore source, fluid evolution and ore precipitation (e.g., Large
111 et al. 2013; Li et al. 2016).

112 The Ordovician turbidite-hosted Chang'an gold deposit (with reserves of > 30 tons
113 Au) occurs in the southern segment of the Ailaoshan belt, SW China (Fig. 1a; Yang et
114 al. 2010, 2011; Zhang et al. 2014a). It is one of the rare examples, globally, of an
115 orogenic gold deposit hosted in a Cenozoic orogenic belt (Goldfarb et al. 2001; Deng
116 et al. 2016, 2019b; Li et al. 2019b; Wang et al. 2019, 2020). Although different studies
117 focusing on the fluid source and ore genesis at Chang'an have been carried out, they
118 are still under debated. Characteristics of intermediate to low temperature (200–280 °C)
119 and salinity (8–18 wt% NaCl equiv) from studies of fluid inclusions of quartz and $\delta^{34}S$

values of whole pyrite (–2.0 ‰ to +3.6 ‰) at Chang'an have been interpreted to be a magmatic source associated with an epithermal gold genesis (Chen et al. 2010; Tian et al. 2014). Based on features of turbidite-hosted disseminated ore, $CO_2$-rich (~3.8–21.2 %) ore fluids and $\delta^{34}S$ values of whole pyrite (+1.1 ‰ to +2.9 ‰), Li et al. (2011) suggested that the Chang'an gold deposit is intermediate between Carlin-type and orogenic gold deposits with magmatic fluids. Based on LA-ICP-MS trace element analysis of pyrite, Zhang et al. (2014a) extrapolated that trace element-poor pyrite in syenite and trace element-rich pyrite in turbidite were formed by magmatic and metamorphic fluids, respectively, and thus considered multiply sourced fluids (metamorphic and magmatic) responsible for the Chang'an gold deposit. In this contribution, based on new observations on the deposit geology, textural and trace element analysis of pyrite, *in situ* S–Pb isotopes of sulfides, pyrite He–Ar isotopes and carbonate C–O isotopes, we provide systematic evidences for the mechanism of fluid–wall-rock reaction that promoted metal precipitation, and further demonstrate that sediment-hosted disseminated ores at Chang'an may be sourced from both deeply sourced fluids and local wall-rock, in contrast to two popular but contrasting origin: local metamorphic devolatilization or deep source.

## Regional Geology

The NW-trending Ailaoshan belt is a Paleo-Tethyan suture zone separating the South China block from Indochina block (Wang et al. 2014; Deng et al. 2014; Yang et al. 2018; Fig. 1a). During the Neoproterozoic, the South China block went through oceanic

subduction, which triggered formation of a series of magmatic arcs along the western margin of the block (Cai et al. 2014). From Cambrian to Devonian, the South China block was situated along the margin of Gondwana and comprised passive continental margin sedimentary sequences (YNGMR 1990; Wang et al. 2014). As a result of opening of the Paleo-Tethys during the Silurian to Devonian, the Ailaoshan Paleo-Tethyan Ocean developed between the South China and Indochina blocks and the clastic rock sequences were deposited along the western margin of the South China block and the eastern margin of the Indochina block (YNGMR 1990; Yang et al. 2018). Southwest-directed (current direction as reference) subduction of the Ailaoshan Paleo-Tethyan oceanic crust and subsequent collision of South China and Indochina blocks determined the NW-trending structural framework (e.g., fold and thrust system, Faure et al. 2016) and formed the arc, syn- and post-collisional magmatic rocks mainly distributed in the eastern margin of the Indochina block (Liu et al. 2015a; Yang et al. 2018).

In the early stage of the continent-continent collision between India and Asia (Yin and Harrison 2000; Chung et al. 2005), the Ailaoshan belt evolved to be a metamorphic core complex belt comprising high-grade metamorphic core constrained by the Ailaoshan and Red River faults (Fig. 1b) and low-grade metamorphic or unmetamorphosed cover (Schärer et al. 1994; Jolivet et al. 2001; Anczkiewicz et al. 2007; Searle et al. 2010). The metamorphic core complex contains high-grade metavolcanic and metasedimentary rocks, including gneiss, amphibolite, and schist with predominantly Proterozoic protoliths and also some igneous protoliths of Triassic

to Cenozoic age (Leloup et al. 1995; Carter et al. 2001; Burchfiel et al. 2008; Liu et al. 2013). The rocks experienced peak amphibolite-granulite facies metamorphism associated with crustal anatexis at 44–36 Ma and post-peak near-isothermal decompression occurred at 32–25 Ma, which was followed by late retrograde metamorphism at 25–14 Ma (Liu et al. 2013, 2015a). The low-grade metamorphic or unmetamorphosed cover is further subdivided into a Paleo-Tethyan arc magmatic belt in the Indochina block and the Jinping terrane in the South China block (Fig. 1b; Wang et al. 2014). Alkali-rich porphyry and lamprophyre dykes formed between ca. 36 and ca. 30 Ma as a result of melting of lower crust and enriched mantle, respectively, in the Ailaoshan belt (Wang et al. 2001; Deng et al. 2015). Major ductile shearing with a large sinistral displacement occurred between ca. 30 and ca. 22 Ma, as indicated by U–Pb zircon ages of pre-, syn-, and post-tectonic leucogranites (Chung et al. 1997; Cao et al. 2012; Liu et al. 2015b). The Ailaoshan belt has developed two-stage rapid exhumation cooling at ca. 27–17 Ma and ca. 14–13 Ma (zircon U-Th-He and apatite fission track; Wang et al. 2016). The metamorphic core complex was extruded upward along pre-existing NW-trending thrusts during in a transpressional setting and exposed by regional exhumation (Burchfiel et al. 2008).

The Chang'an gold deposit is located in the low-grade Jinping terrane, which is bound by the Ailaoshan fault to the east and Tengtiaohe fault to the west (Fig. 1b). Strata exposed in the terrane are mostly Ordovician to Triassic and Quaternary (Fig. 1b). The Ordovician and Silurian strata are composed of turbidite packages and carbonate, respectively (YNGMR 1990). Magmatic rocks occurring in the easternmost

part of the Jinping terrane are Neoproterozoic intrusions that form the basement to Phanerozoic successions (Fig. 1b). Lamprophyre dikes (Chen et al. 2014) and alkali-rich porphyries associated with porphyry/skarn mineralization (Zhu et al. 2009; Zhang et al. 2014b) were widely intruded in the Jinping area (Fig. 1b). The timing of mineralization in the Chang'an gold deposit has not been constrained precisely. Some researchers considered that the Chang'an gold deposit shares a similar age with the Tongchang porphyry deposit with age of ca. 34 Ma (molybdenite Re-Os dating; Wang et al. 2005) due to their close proximity (< 1.5 km). Based on a paleomagnetic study, Gao et al. (2018) interpreted gold mineralization at Chang'an to post-date large-scale sinistral shearing along the Ailaoshan shear zone (ca. 30–22 Ma; Liu et al. 2015b).

## Deposit Geology

### Lithologic units

The sedimentary units mainly consist of an Ordovician turbidite package and Silurian dolostone (Fig. 2a, b). The Ordovician sequence trends NE to EW with northwest to northerly dip and is exposed in the eastern and western parts of the mining area (Figs. 3, 4a). The Silurian rocks trend EW and are exposed in the middle part of the mining district (Fig. 2a). The Ordovician turbidite packages include a thick sequence of sandstone with minor thin layers of carbonaceous and calcareous sandstone, siltstone, mudstone and conglomerate (YNGMR 1990). The Silurian sequence, dominated by dolostone, unconformably overlies the Ordovician rocks (Fig. 3). The Palaeozoic sedimentary rocks are cut by both NE- to E-trending lamprophyre dikes (35.16 ± 0.16

208 Ma; biotite Ar-Ar plateau age; Wang, 2008), and NE- to E-trending and NW-trending
209 syenite dikes (ca. 34−35 Ma; zircon U-Pb dating; Zhang et al. 2017) (Figs. 2a, 3, 4b).
210 The syenite dikes cut the lamprophyre dikes (Fig. 4b). The Ordovician turbidite,
211 especially the sandstone, is the main host for orebodies with minor occurrences in the
212 syenite (Fig. 2a, b).
213

214 **Structural setting and orebody occurrence**

215 The Chang'an fault, which dips at ~75° towards ~070° in the vicinity of the Chang'an
216 gold deposit (Figs. 3, 4c), is a splay of the regional-scale Ganhe fault (Figs. 2a). The
217 Chang'an fault is developed mainly within the Silurian dolostone and locally along the
218 unconformity boundary between Ordovician turbidite and Silurian dolostone (Fig. 2a).
219 The fault zone is 150−200 m wide and consists of a 10−30 m wide core central to a
220 60−80 m wide zone of cataclastic deformation in the Silurian dolostone and 80−100 m
221 wide zone of cataclastic deformation in the Ordovician sandstone (Figs. 2a, b, 3). The
222 lamprophyre and syenite dikes in the fault zone have also been deformed to cataclastic
223 rocks (Figs. 3, 4b). Sinistral-reverse displacement on the Chang'an fault is inferred from
224 the striations and steps on the fault planes and the secondary faults (Fig. 4c, d).
225 Orebodies occur within the Chang'an fault zone and are distributed in the hanging wall
226 cataclastic sandstone zone (Fig. 2a, b). The orebodies, occurring as lenticular,
227 stratiform-like and podiform in shape, show a NW trend with a dip of 70~80° to NE,
228 and taper out towards the east (Fig. 2a, b). They are discontinuous over 1.8 km along
229 strike and 20 to 253 m down dip with average thickness of 16 m and average grade of

4.54 g/t (Zhang et al. 2014). Ore shoots are mainly distributed around the intersection between secondary faults and the contact between Ordovician turbidites and intrusions (syenite and lamprophyre) (Fig. 3).

## Alteration

The alteration types at Chang'an include silicification, sericitization, sulfidation, and carbonation (Fig. 5a-f), which are found in the Ordovician turbidite, Silurian dolostone, lamprophyre and syenite in the hanging wall of the Chang'an fault with no obvious zonation (Fig. 2a, b). In the turbidite (dominated by sandstone), the silicification and sericitization show a pervasive distribution along microfractures (Fig. 5a, b). The quartz and sericite arising from alteration are commonly distributed in pressure shadows at crystal terminations of pyrite (Fig. 5a). In the lamprophyre and syenite, the sericite and quartz together with pyrite, ankerite, apatite and rutile were preferentially developed along the biotite cleavage and grain boundaries (Fig. 5c, d). Sulfidation (sulfides; e.g. pyrite, arsenopyrite, etc.) mainly occur in the sandstone-hosted cataclastic zone (Fig. 5a, b, e, f). Two stages of carbonation including phases of calcite and ankerite may be identified in all rock types, i.e., intergrowth with sulfidation (Fig. 5e) and cross-cutting sulfidation (Fig. 5f).

## Samples and Analytical Techniques

### Sample preparation

Forty-three samples of pre-ore and different hydrothermal stages were collected for this study (Fig. 3). Thirty-five thin sections and nineteen polished mounts from different spatial locations were prepared for mineralogical and textural studies. Nine polished mounts from orebodies (CA20, CA33, CA36, CA38 and CA39) and weakly mineralized turbidite sequence (CA21 and CA25) and syenite (CA1 and CA29) (Fig. 3) were further selected for analyses of trace elements and S–Pb isotopes of sulfides (pyrite and arsenopyrite). Trace element and Pb isotope of sulfides were analyzed by laser ablation-inductively coupled plasma-mass spectrometry (LA-ICP-MS), and S isotopes in sulfides were analyzed using sensitive high-resolution ion microprobe (SHRIMP). Four pyrite samples from hydrothermal stage II (CA17, CA31, CA34 and CA35) were separated by hand-picking (60–80 mesh size; 99% purity) for He–Ar isotope analysis. Four calcite samples from stage II (CA22B, CA24B, CA27B and CA37B) and six from stage III (CA22N, CA24N, CA27N, CA33N, CA37N and CA38N) (Fig. 3) were hand-picked under a binocular microscope with the purity of 99% for C–O isotope analysis.

### Morphology and composition analysis of sulfides

Polished thin sections and mounted blocks of ore samples were examined under optical microscope to study the morphological and paragenetic features of the sulfides. The samples were further examined using a scanning electron microscope (SEM) to

identify compositional zoning and micro-textures. The SEM analysis was carried out at the Key Laboratory of Deep-Earth Dynamics, Institute of Geology, Chinese Academy of Geological Sciences, using the FEI Nova NanoSEM 450. The back scattered electron (BSE) images were taken under operating voltage of 15-20 KV and the working distance of 13.5 mm.

**LA-ICP-MS trace element analyses**

The trace element compositions of pyrite and arsenopyrite were analyzed at the LA-ICP-MS facility at the University of Tasmania using a 213-nm solid-state laser microprobe (UP213, NewWave Research) coupled to an Agilent 7500a quadruple mass spectrometer. The LA-ICP-MS spot and mapping data may be used to characterize spatial and temporal variations in the trace element composition of the sulfides (Large et al. 2009).

Because of the range of grain sizes, the beam size for spot analyses of pyrite and arsenopyrite was kept as 29 µm and 19 µm, respectively. Laser repetition rate was typically 5 Hz and laser beam energy at the sample was maintained at 2.7 J/cm$^2$. The analysis time for each spot was 90 s, comprising a 30-s measurement of background (laser off) and a 60-s analysis of the sample (laser on). The analyses were carried out in an atmosphere of pure He, which was introduced into the cell at a rate of 0.8 l/min. To improve aerosol transport, 0.85 l/min of Ar was mixed with the He carrier gas. Calibration standards STDGL3, GSD-1G and PeruPy (Belousov et al. 2015) were analyzed twice between every 31 unknown analyses and between each sample change.

Geometric mean of detection limit for $Co^{59}$, $Ni^{60}$, $Cu^{65}$, $Zn^{66}$, $As^{75}$, $Se^{77}$, $Mo^{95}$, $Ag^{109}$, $Sb^{121}$, $Te^{125}$, $Au^{197}$, $Tl^{205}$, $Pb^{208}$ and $Bi^{209}$ selected for following discussion are 0.01 ppm, 0.01 ppm, 0.76 ppm, 0.42 ppm, 3.58 ppm, 6.75 ppm, 0.004 ppm, 0.01 ppm, 0.05 ppm, 0.21 ppm, 0.007 ppm, 0.01 ppm, 0.03 ppm and 0.002 ppm, respectively.

Line and image analyses were performed under similar conditions except that a 11-μm spot size and 10-Hz pulse rate were used. Instead of individual spot locations, a series of parallel lines were ablated at a speed of 11 μm/s. The detailed process for creating a trace element map may be found in Steadman et al. (2013).

## SHRIMP S isotope

*In situ* SHRIMP S-isotopic analysis of pyrite and arsenopyrite was undertaken at the Research School of Earth Sciences, Australian National University. A 25 μm spot size and ~1 μm beam depth were used for all samples, regardless of grainsize. The Ruttan pyrite, with a $\delta^{34}S_{V\text{-}CDT}$ (Vienna-Canyon Diablo Troilite) values of +1.2 ‰ (Crowe and Vaughan 1996), was used as a primary standard to normalized all analyses. Errors for each sulfur isotope ratio are reported at the 2σ confidence level. The analytical errors (2σ) of Ruttan pyrite were ±0.35 ‰ (n=12), and the internal precisions are better than ±0.08 ‰ (Ireland et al. 2014). Data are expressed in delta notation such that ratios are expressed as per mil (‰) deviations from a reference value, e.g.

$$\delta^{34}S = [(^{34}S/^{32}S)_{measured} / (^{34}S/^{32}S)_{reference} - 1] \times 1000$$

where $(^{34}S/^{32}S)_{measured}$ is the measured $^{34}S/^{32}S$ ratio, $(^{34}S/^{32}S)_{reference}$ is the reference value of that ratio used for normalization, and $\delta^{34}S$ is expressed in per mil (‰) deviation.

The detailed analytical procedures are described by Ireland et al. (2014).

## LA-ICP-MS Pb isotope

*In situ* Pb isotope analyses of different generations of pyrites and galena in the Chang'an deposit were analyzed at the University of Tasmania, using a 213-nm solid-state laser microprobe (UP213, NewWave Research) coupled to an Agilent 7500a quadruple mass spectrometer. Laser spot sizes for analyses of pyrite and galena are 74 μm and 29 μm, respectively, and the laser operated at 10 Hz, using fluence at the sample of 2.9 J/cm$^2$. Analytical processes and conditions of the analyses are similar to those described in Woodhead et al. (2009). The NIST610 and STDGL3 glasses (Belousov et a. 2015), and Chatree and Jaguar pyrites (Woodhead et a. 2009) were used as calibration standard for pyrite, whereas the MtMurch and BH galena together with STDGL3 glass (Belousov et a. 2015) were used as calibration standard for galena.

## He−Ar isotopes

Measurements of He and Ar isotopes were conducted at the Institute of Geology and Geophysics, Chinese Academy of Sciences in Beijing, using the Noblesse mass spectrometer. The Noblesse instrument with >700 mass resolution is sufficient to allow complete separation of $^3$He and HD. The operating and data processing procedures were similar to those described by He et al. (2011).

Post-mineralization structural overlap cannot be found in veinlet-hosted mineralization in hydrothermal stage II, thus fluid inclusions from pyrite (py$_{II-1}$ and py$_{II-}$

335 $_2$) in stage II may characterize the He−Ar isotopic composition of this stage. The
336 veinlets were separated from wall-rocks and then crushed and sieved to pass the 80–
337 100 mesh fractions. Fresh pyrite crystals were picked by hand and washed with acetone
338 in an ultra-sonic bath for 10 min. The grains were then rinsed in the ultra-sonic bath
339 several times with distilled water and dried. Approximately 1 g of sample was loaded
340 into the in vacuum crusher. Samples were transferred to an oven and roasted under
341 conditions of 130 °C in the purification system for two or three days to remove the
342 atmosphere attached to the surface of the samples. The mineral grains were crushed by
343 a one-step or multistep process in a vacuum crusher at about 1500 psi to extract the
344 noble gases. The Ar in the noble gas mixtures was trapped in a cold finger with charcoal
345 at the temperature of liquid nitrogen. Helium was trapped in another cold finger at about
346 10 K and released at 35 K.

347 **C−O isotopes**

348 The $\delta^{13}C$ and $\delta^{18}O$ compositions of calcites formed in stages II and III were measured
349 by GasBench coupled with Thermo Finnigan Delta V Advantage at Oxy-Anion Stable
350 Isotope Consortium (OASIC) at Louisiana State University. About 0.20 mg samples
351 were loaded into 12 mL Labco Exetainer vials and sealed with Labco septa were flushed
352 with 99.999% Helium and automatically acidified at 70 °C. The carbon dioxide analyte
353 gas was isolated via gas chromatography, and water was removed using a Nafion trap.
354 Isotopic results are expressed in the delta notation as per mil (‰) deviations from the
355 V-PDB standard. Precisions for $\delta^{13}C$ and $\delta^{18}O$ are routinely better than 0.06 ‰ and
356 0.09 ‰, respectively.

## Paragenesis and Pyrite Generations

Pre-ore pyrite, termed as $py_s$, is composed of layered or banded concentrations of porous pyrite or pyrite nodules parallel to the bedding of the Ordovician sequence (Fig. 4a; Table 1). The pyrite nodules are formed by dense aggregates of 5–200 μm euhedral to subhedral crystals (Fig. 6a). The porous $Py_s$ occur as subhedral pyrite varying from 20 to 1000 μm across (Fig. 6b, c, d).

Based on the mineral paragenesis and cross-cutting relationships, three distinct hydrothermal stages are recognized, namely: stage I quartz–arsenopyrite–pyrite, stage II quartz–calcite–polymetallic sulfides and stage III quartz–calcite. Hydrothermal stage I is represented by disseminated distribution of quartz–arsenopyrite–pyrite, and three generations of pyrite have been identified in stage I: $py_{I\text{-}1}$ and $py_{I\text{-}2}$ in turbidite (especially sandstone), and $py_{I\text{-}Sy}$ in the syenite (Figs. 3, 6b-d; Table 1). $Py_{I\text{-}1}$ has a pervasive distribution in the sandstone and is composed of euhedral-subhedral crystals ranging from 20 to 200 μm across. $Py_{I\text{-}1}$ commonly develops oscillatory zoning structure and overgrows $py_s$ with irregular contact boundaries (Figs. 6c, 7b). It shows fine-grained porous texture that is commonly filled with anhedral quartz, arsenopyrite, galena, chalcopyrite and electrum inclusions (Fig. 6a-d). $Py_{I\text{-}Sy}$ is euhedral-subhedral, unzoned pyrite with 20 to 150 μm across and contains similar mineral inclusions (such as fine-grained quartz, arsenopyrite and galena) to $py_{I\text{-}1}$ (Fig. 7a). $Py_{I\text{-}2}$ with 20 to 50 μm across occurring in the sandstone generally overgrows $py_{I\text{-}1}$ as thin rim to produce euhedral grains, and rarely contains base-metal mineral inclusions (Fig. 6d; Table 1).

379 Hydrothermal stage II occurs as quartz–calcite–polymetallic veinlets controlled by
380 the NW-, NE- and EW-trending faults (Fig. 4e, f), which crosscut the syenite and
381 lamprophyre (Fig. 4b). Two generations of pyrite, named $py_{II-1}$ and $py_{II-2}$, may be
382 identified in stage II (Fig. 7b, c) and crosscut $py_{I-1}$ and $py_{I-2}$ (Fig. 7b). $Py_{II-1}$ is subhedral
383 crystal with 20 to 150 μm across and generally has porous textures with abundant
384 inclusions of galena, sphalerite, and tetrahedrite (Fig. 7b, c). $Py_{II-2}$ is euhedral with 30
385 to 200 μm across and commonly overgrows $py_{II-1}$ (Fig. 7b, c). $Py_{II-2}$ is cogenetic with
386 euhedral galena, chalcopyrite, sphalerite, tetrahedrite and proustite (Fig. 7c, d).
387 Hydrothermal stage III is dominated by NW-trending quartz and calcite veinlets with
388 only minor sulfides (Figs. 3, 4g). The mineral paragenesis during pre-mineralization
389 and different hydrothermal stages are summarized in Fig. 8 and Table 1.
390

391 **Results**

392 **Trace element compositions**

393 Data analyzed by 77 spots and 2 lines (one crosscuts $py_{I-1}$ and $py_s$ in sample CA20
394 and the other crosscuts $py_{II-2}$ and $py_{II-1}$ in sample CA38; Fig. S1) include 14 analyses of
395 $py_s$, 23 of $py_{I-1}$, 17 of $py_{I-Sy}$, 4 of $py_{I-2}$, 14 of $py_{II-1}$, 9 of $py_{II-2}$ and 13 of arsenopyrite.
396 Results of LA-ICP-MS spot and line analyses are given in Table S1 and selected trace
397 element compositions of different generation of pyrites and arsenopyrite are illustrated
398 in Table 2. $Py_s$ contains a wide range of trace elements, the most abundant of which are
399 As (geometric mean 620.8 ppm), Pb (61.6 ppm), Ni (59.8 ppm), Mo (54.4 ppm), Co
400 (23.4 ppm), Cu (13.0 ppm), Se (8.3 ppm), Sb (4.8 ppm), Tl (4.1 ppm), Zn (4.1 ppm),

This is the peer-reviewed, final accepted version for American Mineralogist, published by the Mineralogical Society of America.
The published version is subject to change. Cite as Authors (Year) Title. American Mineralogist, in press.
DOI: https://doi.org/10.2138/am-2020-7508. http://www.minsocam.org/

401 Te (3.3 ppm), Bi (0.7 ppm) and Ag (0.4 ppm) with geometric mean Au/Ag of 0.1 (Table
402 2). Notably, $py_s$ contains low Au content ranging from below detection limit to 0.46
403 ppm (geometric mean of 0.06 ppm; standard deviation (S.D.) of 0.2) and highly variable
404 As (2.3–10371 ppm; S.D.=3569.2) (Table 2). $Py_{I-1}$ has significantly elevated trace
405 elements, except Mo, Te and Tl, compared to $py_s$ (Fig. 9; Figs. S1-3). The Au content
406 in $py_{I-1}$ ranges from 0.6 to 227.1 ppm (geometric mean=8.9 ppm; S.D.=63.2) (Table 2).
407 Other elevated trace elements include As (geometric mean 8931 ppm), Ni (248.1 ppm),
408 Cu (139.9 ppm), Pb (120.0 ppm), Co (79.8 ppm), Sb (26.2 ppm), Zn (8.4 ppm) and Ag
409 (8.2 ppm) with geometric mean Au/Ag of 1.2 (Table 2).

410 Arsenopyrite contains As (geometric mean 474554 ppm) and much higher Pb (347.2
411 ppm), Au (268.8 ppm; S.D.=155.6), Cu (239.1 ppm) and Sb (73.1 ppm) with Au/Ag of
412 22.6, but lower Ni (113.9 ppm) and Co (26.1 ppm) than $py_{I-1}$ (Table 2). In sharp contrast,
413 $py_{I-Sy}$ has much lower trace element contents relative to $py_{I-1}$ and arsenopyrite (Fig. 10;
414 Fig. S4), such as As (geometric mean 1131 ppm), Ni (63.0 ppm), Co (62.7 ppm) and Pb
415 (8.6 ppm) with mean Au/Ag of 0.3 (Table 2). The Au content in $py_{I-Sy}$ ranges from
416 below detection limit to 2.3 ppm with a geometric mean value of 0.4 ppm. Similarly,
417 $py_{I-2}$ has lower Au (0.5 to 2.4 ppm; geometric mean 0.4 ppm; S.D.=0.7) and other trace
418 elements, such as As (2183 ppm), Ni (44.8 ppm), Co (21.7 ppm) and Pb (27.7 ppm)
419 (Table 2), which is similar to those of $py_{I-Sy}$ but lower than those of $py_{I-1}$ and
420 arsenopyrite (Fig. 10). LA-ICP-MS images of pyrite from stage I also reveal spectacular
421 compositional zoning patterns (Fig. 9; Figs. S2-3), which correspond to distinct
422 generations of pyrite revealed by BSE petrographic observation. Figure 9 highlights

three generations of a selected pyrite grain: the core ($py_s$) has low Au, As, Sb, Pb, Cu but high Co, Ni, Bi and Te, whereas the inner rim ($py_{I-1}$) enriches in Au, As, Ag, Co, Ni, Sb, Pb, Cu and Bi, and the thin outer rim ($py_{I-2}$) contains much lower trace elements compare to $py_{I-Sy}$.

$Py_{II-1}$ contains higher As (geometric mean 11325 ppm), Pb (1061 ppm), Cu (558 ppm), Sb (241.7 ppm), Zn (63.4 ppm) and Ag (58 ppm), but lower Au (1.0 to 34.8 ppm with a geometric mean value of 4.1 ppm; S.D.=9.7) and Au/Ag (geometric mean=0.1) relative to $py_{I-1}$ (Table 2). $Py_{II-2}$ contains As (geometric mean 6311 ppm), Pb (98.5 ppm), Ni (26.6 ppm), Cu (19.5 ppm), Sb (16.8 ppm), Ag (11.7 ppm), Co (8.0 ppm), Zn (6.8 ppm) and Au (geometric mean 2.3 ppm; S.D.=4.6), all much lower than values of $py_{II-1}$ (Table 2). The spot and line analysis results for $py_{II-1}$ to $py_{II-2}$ are consistent with their LA-ICP-MS spectra (Fig. 10). Figure 10 shows a porous core ($py_{II-1}$) with galena and Au-bearing polybasite inclusions enriched in As, Pb, Cu, Sb, Ag and Zn, and a rim ($py_{II-2}$) contains lower contents of these elements compared with $py_{II-2}$. Plots based on Au-As relationship of aforementioned arsenian pyrites of different generations at Chang'an fall below the gold saturation line of Reich et al. (2005) (Fig. 11a), indicating that the gold is most probably held within the structure of the arsenian pyrite and arsenopyrite. The pattern of the As-Au data in Figure 11a for $py_{I-1}$, strongly suggests that the gold saturation line for the Chang'an deposit is about an order of magnitude lower in Au than for Carlin-type deposits as defined by Reich et al (2005). This difference in the position of the gold saturation line has been noticed by Large and Maslennikov (in press) for several other orogenic gold deposits.

### *In situ* S-isotope analyses

The SHRIMP S-isotopic data for arsenopyrite and the different generations of pyrite are shown in Table S2 and plotted in Figure 12. The $\delta^{34}S$ values of thirteen analyses of $py_s$ show a fairly wide range of –18.1 to +30.4 ‰ with mean value of +1.9 ‰ (n=20), respectively. In hydrothermal stage I, twelve analyses of $py_{I-1}$ grains yielded a relatively restricted $\delta^{34}S$ range of –3.2 to +3.3 ‰ with a mean of +0.6 ‰ and seven analyses on $py_{I-Sy}$ grains gave a $\delta^{34}S$ range of +0.6 to 6.3 ‰ (mean = 3.4 ‰). The six $\delta^{34}S$ values of arsenopyrite range from +3.0 to +7.1 ‰ (mean = +4.6 ‰; Table S2). The $\delta^{34}S$ values of three analyses of $py_{I-2}$ range from –2.8 to +0.2 ‰ (mean = –1.1 ‰). In hydrothermal stage II, $\delta^{34}S$ values of $py_{II-1}$ range from –2.8 to +1.2 ‰ (mean = –1.2 ‰, n=8), which are slightly higher than those of $py_{II-2}$ with a range from –6.2 and –0.8 ‰ (mean = –3.6 ‰, n=10) (Table S2; Fig. 12).

### *In situ* Pb isotope

*In situ* Pb isotopes of different generations of pyrites and galena in the Chang'an deposit are shown in Table S3 and Figure 13. $Py_s$ have $^{206}Pb/^{204}Pb$ of 18.88–19.19 (average 19.05), $^{207}Pb/^{204}Pb$ = 15.76–16.01 (average 15.86), and $^{208}Pb/^{204}Pb$ = 38.55–40.20 (average 39.87, n=5; Table S3). In hydrothermal stage I, Pb isotope ratios of $py_{I-1}$ are 18.98–19.31 (average 19.15) for $^{206}Pb/^{204}Pb$, 15.85–15.90 (average 15.87) for $^{207}Pb/^{204}Pb$ and 38.37–39.91 (average 39.64, n=2), which have overlapped ranges of those of $py_{I-Sy}$ but slight lower average values than those of $py_{I-Sy}$ (Table S3; Fig. 13). Pb isotope ratios of galena in hydrothermal stage II fall in a limited range as follows: $^{206}Pb/^{204}Pb$ = 18.75–18.89 (average 18.84), $^{207}Pb/^{204}Pb$ = 15.63–15.71 (average 15.67),

and $^{208}Pb/^{204}Pb$ = 38.01–39.41 (average 39.25, n=12; Table S3), which have generally lower average Pb isotope ratios compared to those of $py_s$, $py_{I\text{-}1}$ and $py_{I\text{-}Sy}$ (Fig. 13).

### He–Ar isotopes

Results of pyrite He–Ar isotopes in stage II are shown in Table S4. The corresponding R/Ra are 0.38 to 0.98 (average = 0.73). The $^{40}Ar/^{36}Ar$ and $^{40}Ar^*/^4He$ ratios show ranges of 353.9 to 959.4 (average = 606.93) and 0.50 to 1.34 (average = 0.89), respectively (Fig. 14a), where $^{40}Ar^*$ represents the $^{40}Ar$ content corrected for atmospheric contribution.

### C–O isotopes

Carbon and oxygen isotopic compositions for calcites from stages II and III are listed in Table S5 and plotted in Fig. 14b. The $\delta^{13}C_{PDB}$ and $\delta^{18}O_{PDB}$ of calcites in stage II are –8.7 to -4.4 ‰ and 9.0 to18.4 ‰, respectively, whereas those in stage III separately range from –4.7 ‰ to 2.7 ‰ and from 8.1 to 25.6 ‰ (Table S5). It is shown that the $\delta^{13}C_{PDB}$ and $\delta^{18}O_{PDB}$ of most calcites in stage III are slightly higher than those in stage II (Fig. 14b).

## Discussion

### Genetic classification

The geological and geochemical features of mineralization in the Chang'an gold

deposit include: (1) proximity to the major lithospheric-scale Ailaoshan shear zone (Fig. 1) but hosted by second- or third-order structures (e.g., the Chang'an fault; Fig. 2a); (2) ore bodies thicken in the fault bend where the fault dip becomes more gentle; (3) gold-related alteration dominated by silicification, sericitization, sulfidation and carbonation (Fig. 5a-f); (4) lack of lateral metal zoning; and (5) trace element association of Au–As with low Ag, Cu, Zn and Pb contents (Fig. 10). These characteristics are inconsistent with the epithermal (e.g., cryptocrystalline silicification and clayization alteration with featured minerals of adularia/alunite/kaolinite; Sillitoe 1997; Hedenquist et al. 2000) and Carlin-type (e.g., decarbonation and argillization alteration and fuzzy gold-pyrite rim; Cline et al. 2005; Wang and Grove 2018) gold deposits, but consistent with those of orogenic gold deposit as summarized by Groves et al. (1998, 2003), Kerrich et al. (2000), and Goldfarb et al. (2005). These features, together with the moderate to low (200–280 °C) mineralization temperature and depths of ~3 km (Chen et al. 2010), suggest a sediment-hosted epizonal orogenic gold affiliation for this deposit.

## Pre-ore pyrite formation

Distribution of $py_s$ parallel to the bedding of Ordovician strata indicates a syn-sedimentary origin for $py_s$. The Ordovician global ocean anoxic events (Strauss 2006), were favorable for trace elements (As, Pb, Ni, Mo, Co, Cu, Se, Sb, Tl, Zn and Te; in decreasing order) to be preferentially partitioned into arsenian pyrites (e.g., Large et al. 2014). $\delta^{34}S$ values of $py_s$ show a wide range of –18.1 to +30.4 ‰ (Table S2; Fig. 12), which is consistent with syn-sedimentary pyrites with large $\delta^{34}S$ range (e.g., Large et

al. 2013; Gregory et al. 2019; Mukherjee et al. 2019). The highest $\delta^{34}S$ values of ~30 ‰ is compared with that of Ordovician global seawater sulfate (Chang et al. 2008). Such large $\delta^{34}S$ range and occurrence of negative $\delta^{34}S$ values can be explained as bacterial sulfate reduction in a marine sedimentary environment (Canfield and Thamdrup 1994; Habicht and Canfield 1997; Canfield 2001). $Py_s$ has relatively high radiogenic Pb isotope ratios plotting above the upper crust curve of Zartman and Doe (1981) (Fig. 13), which may be attributed to the radioactive decay of U and Th of the organic matter in the Ordovician strata.

## Texture and chemical evolution of pyrite

Based on textural observation and LA-ICP-MS data of pyrite, the textural evolution of pyrite at Chang'an, from $py_{I-1}$ to $py_{II-2}$, correlates to the systematic changes in gold and other trace metal concentrations in pyrite, indicating two pulses of metal enrichment. During the early fluid pulse (i.e., hydrothermal stage I), oscillatory-zoned $py_{I-1}$ (Figs. 6c, 7b), accompanied by quartz grains with pressure shadow structures (Fig. 5a), was precipitated. LA-ICP-MS data shows an Au, As, Cu and Sb oscillatory zoning (Fig. 9), and Au shows a positive relationship with As, Cu and Sb (Fig. 11a, b, d). The LA-ICP-MS element maps in Figure 9 show that whereas the As and Sb are uniformly distributed through $py_{I-1}$, the maximum gold band (10 – 70 ppm Au) is much thinner and concentrated on the outer part of the $py_{I-1}$ As-Sb growth zone. $Py_{I-1}$ is enriched in As, Ni, Cu, Pb, Co, Sb, Au, Zn and Ag (in decreasing order; Table 2; Fig. 9) and contains cogenetic arsenopyrite, galena and electrum inclusions (Figs. 6a-d, 9b, d), indicating

532 that the ore-forming fluid carried these elements noted above. The ubiquitous presence
533 of the Au-As–rich hydrothermal pyrite ($py_{I-1}$) overgrowths on detrital pyrites ($py_s$) (Fig.
534 6a-d) and their uniform trace element composition across all samples studied indicate a
535 uniform deposit-scale As-Au-rich hydrothermal event. The element zoning in $py_{I-1}$ may
536 be explained by two possible scenarios: fluid pressure fluctuation (Sibson and Scott
537 1998; Peterson and Mavrogenes 2014) and crystallographic incorporation of trace
538 elements controlled by growth rate (Barker and Cox 2011; Fougerouse et al. 2016; Wu
539 et al. 2019). Although pressure shadow structure of quartz that intergrown with $py_{I-1}$
540 indicates a possible relationship between structural pressure and formation of $py_{I-1}$ and
541 quartz, lack of direct evidence for pressure fluctuation from fluid inclusion study makes
542 the former not confirm. Similarly, the later cannot be confirmed or excluded at the
543 current scale of observation. Although $py_{I-Sy}$ in the syenite has much lower As, Ni, Co,
544 Pb and Au relative to $py_{I-1}$ (Table 2; Fig. 11), their similar mineral inclusions of fine-
545 grained quartz, arsenopyrite and galena (Figs. 6, 7a), and undistinguishable S and Pb
546 isotope compositions (Figs. 12, 13) indicate that they may be produced by the same ore
547 fluids. Differences in trace element compositions and sulfide texture may be attributed
548 to different wall-rock composition ($py_{I-1}$ in turbidite and $py_{I-Sy}$ in syenite) in which
549 sulfides precipitated (see "Mineralization mechanism" for further discussion). The thin
550 $py_{I-2}$, occurring as $py_{I-1}$ rim in the sandstone (Fig. 6d), contains much lower trace
551 elements (Fig. 9), indicative of a fluid waning of the early hydrothermal pulse.

552 The late hydrothermal pulse is represented by the formation of veinlet-hosted $py_{II-1}$
553 and $py_{II-2}$ in hydrothermal stage II. $Py_{II-1}$ contains galena, chalcopyrite, tetrahedrite,

554 sphalerite and Au-bearing polybasite inclusions (Figs. 7b, c, 10) and is enriched in As,
555 Pb, Cu, Sb, Zn and Ag (in decreasing order) with minor Au (geometric mean 4.1 ppm;
556 Table 2; Fig. 10). Although the trace elements in $py_{II-2}$ is lower than those in $py_{II-1}$ (Table
557 2; Fig. 10), $py_{II-2}$ is cogenetic with abundant euhedral galena, chalcopyrite, tetrahedrite
558 and sphalerite (Fig. 7d). The signatures indicate that the late hydrothermal fluids are
559 As- and base metal-rich but Au-poor. The LA-ICP-MS element images of $py_{II-1}$ show
560 that Ag, Pb, Cu and Sb have a similar distribution (Fig. 10), and appear to be
561 concentrated in cracks, indicating that the elevated base-metal elements are related to
562 micro-inclusions of base-metal sulfides, particularly galena and tetrahedrite in cracks
563 in $py_{II-1}$ (Fig. 10). Two mechanisms may explain the base-metal elements related to
564 galena and tetrahedrite in the cracks: Ag enters into the crystal lattice of galena together
565 with Sb (or Bi) by substitution for Pb as illustrated in the formula $Ag^{+} + (Sb, Bi)^{3+} =$
566 $2Pb^{2+}$ (Li et al. 2016); Ag incorporates into tetrahedrite to form argentiferous
567 tetrahedrite via an Ag–Cu solid-state exchange reaction (Sack et al. 2003). The LA-
568 ICP-MS element images and positive correlations between Pb and Ag, Ag and Sb, and
569 Ag and Cu (Figs. 10d, g, h, i, 11f) support the two interpretations.

570 **Mineralization mechanism**

571 A series of lines of key evidences, including (1) partial replacement textures of $py_s$
572 and irregular contact boundaries between $py_s$ and $py_{I-1}$; and (2) existence of
573 hydrothermal minerals (arsenopyrite, galena, electrum, quartz, calcite, etc.) along the
574 contact boundaries or in the porous $py_s$ and $py_{I-1}$, support an interaction of ore fluids
575 with sedimentary pyrite. The interaction of sedimentary pyrite and ore fluids, and

This is the peer-reviewed, final accepted version for American Mineralogist, published by the Mineralogical Society of America.
The published version is subject to change. Cite as Authors (Year) Title. American Mineralogist, in press.
DOI: https://doi.org/10.2138/am-2020-7508. http://www.minsocam.org/

formation of hydrothermal pyrites plus minor inclusions (Apy, Gn, Ccp and Ele) can be described by:

$Py_s$ + *Au-bearing ore fluids* → *remnant* $py_s$ + $py_{I\text{-}1}$ *(enriched in Au, As, Ni, Cu, Pb, etc)* + *Apy* + *Gn* + *Ccp* + *Ele*

There may be an intermediate step required in the above reaction, i.e., after the initiation of the reaction, a meta-stable pyrite first formed with Au, As, Pb, and Cu dissolved in the structure before it broke down to $py_{I\text{-}1}$ and arsenopyrite, galena, chalcopyrite and electrum (e.g., Stepanov 2019). This step is unequivocally supported by the fact that arsenopyrite, galena, chalcopyrite and electrum are very fine-grained (micro-inclusions) crowded in $py_{I\text{-}1}$ (Fig. 6a-d). The cogenetic gold-bearing arsenian pyrite and arsenopyrite, and hydrothermal calcite (Fig. 5b, e) and rutile in the sandstone (Fig. 9a; Fig. S3) suggest that the ore fluids have also reacted with the Fe carbonate and Fe-Ti oxides in the sandstone. Similarly, unzoned $py_{I\text{-}Sy}$ may be produced by the reaction of ore fluids with biotite in the syenite as evidenced by the replacement of biotite by pyrite and ankerite (Fig. 5d). Different reactors ($py_s$ in the sandstone and biotite in the syenite) may be responsible for differences in trace element compositions and sulfide texture between $py_{I\text{-}1}$ and $py_{I\text{-}Sy}$, such as zoned $py_{I\text{-}1}$ and unzoned $py_{I\text{-}Sy}$ that contains much lower trace elements and finer cogenetic mineral inclusions than $py_{I\text{-}1}$ (Figs. 6, 7a, 11). These reactions indicate that the host rocks could provide part of ore materials in low-grade metamorphic rocks through fluid–wall-rock/mineral interaction rather than metamorphic devolatilization reaction.

598 **Sources of early fluid pulse**

599 **Sulfur isotope.** The Au is hosted by the sulfides, like pyrite and arsenopyrite,
600 implying that ore fluids were enriched in reduced S and that Au was principally
601 transported as an Au-HS complex (e.g., Seward 1991; Stefánsson and Seward 2004;
602 William-Jones et al. 2009). The S isotope ratios thus provide insights into potential Au
603 and ore fluid sources. The S isotope fractionation between pyrite and a reduced
604 hydrothermal fluid is less than 2 ‰ at a temperature of ~250 °C (Ohmoto 1972),
605 consistent with ore-forming temperature of the Chang'an gold deposit (Chen et al.
606 2010). Thus, the $\delta^{34}S$ values of ore sulfides should broadly mimic those of the ore-
607 forming fluids.

608 Au-rich $py_{I-1}$ and arsenopyrite and Au-poor $py_{I-Sy}$ have $\delta^{34}S$ range of –3.2 to +7.1 ‰
609 (Fig. 12), which falls within the normal range between about –15 ‰ and +15 ‰ for
610 sediment-hosted orogenic gold deposits (Chang et al. 2008 and references therein). A
611 homogeneous sulfur isotope composition may only be shifted with few per mil via
612 changes in redox and other thermo-chemical parameters (Goldfarb and Groves 2015;
613 Zhao et al. 2018). Such sulfur isotope composition and range (10.3 ‰) of $\delta^{34}S$ values
614 is inconsistent with a single homogeneous sulfur reservoir, such as magmatic (0 ± 5 ‰)
615 and mantle sulfur (0 ± 3 ‰; Ohmoto and Rye 1979), and is more compatible with, but
616 not diagnostic of, a (meta)sedimentary sulfur source or mixed sulfur source. A
617 comparison between the sulfur isotope data for Chang'an and sea-water sulfate plus
618 global sediment-hosted orogenic gold deposits through time (Fig. 12) shows that the
619 sulfur isotope composition of sulfides in stage I at Chang'an is inconsistent with those

620 in the underlying strata of the Ordovician hosting sequence. Several lines of evidence
621 support that $py_s$ has provided part of trace metals for this stage, as follows: (1) $py_s$
622 contains a suite of As, Pb, Cu, Sb, etc. (Figs. 9, 11); (2) arsenopyrite, galena,
623 chalcopyrite and electrum in stage I are intergrown with $py_{I-1}$ and occur as fine-grained
624 micro-inclusions along contact between $py_s$ and $py_{I-1}$ (Fig. 6a-d); (3) $py_s$ has been partly
625 dissolved by ore fluids, resulting in irregular boundaries (Fig. 6a-d). However, $py_s$ has
626 very low Au content (mean 0.06 ppm), suggesting that external deep Au-bearing fluid
627 is certainly required for gold mineralization in hydrothermal stage I. Therefore, we infer
628 that ore fluids in hydrothermal stage I were sourced from mixing external deep Au-
629 bearing fluids and pre-ore $py_s$. There are two preferred explanations about the external
630 Au-bearing fluids: one is deep metamorphic fluids if the Chang'an gold mineralization
631 was coeval to regional exhumation and cooling of hot metamorphic core complex
632 (720 °C to 760 °C; Liu et al. 2013), which could trigger metamorphic devolatilization
633 of contacted rocks, and the other is metasomatic lithospheric mantle-sourced fluids if
634 the Chang'an gold mineralization is later than regional exhumation and cooling.
635 Paleomagnetic study indicates that gold mineralization at Chang'an postdated large-
636 scale sinistral shearing along the Ailaoshan shear zone (Gao et al. 2018). If this age is
637 valid, the external Au-bearing fluids would be sourced from metasomatic lithospheric
638 mantle as interpreted by Wang et al. (2019). The hydrothermal sulfides in stage I show
639 a narrower $\delta^{34}S$ range (–3.2 to 7.1 ‰) relative to syn-sedimentary pyrite (–18.1 to
640 +30.4 ‰; Fig. 12), demonstrating that the fluid-pyrite interaction has gradually
641 homogenized the sulfur. The homogenization of early sulfur driven by fluid-rock

642 interaction and metamorphism has been reported by Chang et al. (2008).

643 **Lead isotopes.** Lead isotope ratios for $py_{I-1}$ and $py_{I-Sy}$ in hydrothermal stage I plot
644 above the upper crust curve of Zartman and Doe (1981). As shown in Figure 13, $py_{I-1}$
645 and $py_{I-Sy}$ display higher $^{206}Pb/^{204}Pb$ ratios than those of Proterozoic volcanics and
646 alkali-rich porphyry in the Ailaoshan belt and mafic rocks in the vicinity of Chang'an
647 deposit (Zhou et al. 1998; Zhang and Scharer 1999; Lu et al. 2013; Fig. 13). Such Pb
648 isotopic signature rules out the main contribution of metal from these reservoirs. Ranges
649 of Pb isotope ratios of hydrothermal $py_{I-1}$ and $py_{I-Sy}$ at Chang'an are undistinguishable
650 from those of $py_s$ (Fig. 13), indicating that the Pb metal may be sourced from the
651 Ordovician turbidite sequence, which supports the above inference that the Ordovician
652 sequence provided part of metals.

653

654 **Sources of late fluid pulse**

655 **S isotope.** Sulfur isotopic composition ($\delta^{34}S$= –2.8 to +1.2 ‰ with a mean of –1.2 ‰)
656 of $py_{II-1}$ formed in stage II can result from a metamorphic, magmatic (0 ± 5 ‰; Ohmoto
657 and Rye 1979), or mantle S (0 ± 3 ‰; Ohmoto and Rye 1979) source. Relative negative
658 $\delta^{34}S$ values of –6.2 to –0.8 ‰ in $py_{II-2}$ (Fig. 12) can be attributed to the fluid oxidation
659 since the ratio of $H_2S/SO_4^{2-}$ will decrease in the oxidized fluids, resulting in more $^{34}S$
660 to concentrate in $SO_4^{2-}$ and thus more negative $\delta^{34}S$ values in sulfides (e.g., Duuring et
661 al. 2009; Kamvong and Zaw 2009).

662 **Pb isotope.** Lead isotope ratios for galena in hydrothermal stage II plot near the
663 orogen and upper crust curves of Zartman and Doe (1981) (Fig. 13), indicative of a

664 crustal-derived lead source. The $^{207}Pb/^{204}Pb$ and $^{206}Pb/^{204}Pb$ ratios of galena is lower
665 than those of $py_{I-1}$, $py_{I-Sy}$ and $py_s$ (Fig. 13), indicating that ore-forming fluids in stage II
666 have less radiogenic Pb than pre-ore $py_s$ and those in stage I. Higher $^{206}Pb/^{204}Pb$ ratios
667 of galena relative to Proterozoic volcanics (Fig. 13; Zhou et al. 1998) rule out the main
668 contribution of Pb metal from Proterozoic volcanics. In contrast, lead isotope ratios for
669 galena partly overlaps those of Ailaoshan leucogranite, alkali-rich porphyry and mafic
670 rocks in Western Yunnan (Fig. 13; Zhang and Scharer 1999; Lu et al. 2013), suggesting
671 that the Pb metal in stage II possibly share similar source region with these rocks.

672 **He–Ar isotopes.** The 0.38 – 0.98 range (average = 0.73) in R/Ra ratios of pyrite
673 (mixture of $py_{II-1}$ and $py_{II-2}$) at Chang'an are intermediate between the crust R/Ra ratio
674 (0.01 to 0.05 Ra; Tolstikhin 1978) and the sub-continental lithospheric mantle (5 – 6
675 Ra; Dunai and Baur 1995) (Fig. 14a). The He–Ar isotopic composition at Chang'an is
676 different from that in the Macraes gold deposits with crust-dominant helium source
677 (Goodwin et al. 2017) and that in the Dongping gold deposit with mantle-dominant
678 helium source (Mao et al. 2003), but consistent with those in the Murantau, Daping and
679 Zhenyuan gold deposits with a mixed crust-mantle helium source (Burnard et al. 1999;
680 Graupner et al. 2006; Sun et al. 2009). This signature could be explained by two
681 possible scenarios: a mixed crust-mantle source, or mantle source with wall-rock
682 contamination. The R/Ra ratios have been used to estimate the proportion of mantle and
683 crustal components in fluids (Li et al. 2010). Using 5.5 Ra and 0.03 Ra as representative
684 of mantle and typical crustal He respectively, a proportion of mantle He between 6 %
685 and 17 % is estimated.

686 **C–O isotopes.** The $\delta^{13}C_{PDB}$ of calcites in hydrothermal stages II and III range from
687 –8.7 to +2.7 ‰ (Fig. 14b), which are consistent with those for most orogenic gold
688 deposits (−23 to +2 ‰; Ridley and Diamond 2000 and reference therein). The calcite
689 $\delta^{13}C_{PDB}$ values at Chang'an are lower (except one value of +2.7 ‰) than those of
690 seawater (0 ‰; Ohmoto and Rye 1979), much higher than those of reduced carbon in
691 sedimentary or metamorphic rocks (−25 ‰; Hoefs 1997), and close to but slightly
692 higher than those of magmatic fluids and mantle (−7 to −2 ‰; Deines et al. 1991;
693 Cartigny et al. 1998). Figure 14b shows that the $\delta^{13}C_{PDB}$ and $\delta^{18}O_{PDB}$ values are
694 intermediate between the fields of sedimentary carbonates and mantle carbonates.
695 Sulfur isotopes of $py_{II-1}$, He–Ar isotopes of fluid inclusions released from pyrite
696 (mixture of $py_{II-1}$ and $py_{II-2}$) and C–O isotopes of calcites suggest that the ore-forming
697 materials in hydrothermal stage II have mantle contributions.
698

699 **Two fluid pulses from distinct systems or an evolving fluid system**

700 The field, textural, compositional and isotopic data support that the two fluid pluses
701 in stages I and II at Chang'an may have been derived from both two distinct fluid
702 systems and from a single, evolving hydrothermal system. These signatures are listed
703 as follows: (1) Au-rich $py_{I-1}$ in stage I is characterized by pervasive disseminated
704 distribution (Fig. 2b) and oscillatory zoning (Figs. 6c, 7b), whereas mineralization in
705 stage II is hosted in veinlets (Fig. 4e, f), which cuts across the mineralization in stage I
706 (Fig. 7c); (2) the ore assemblage in stage I is dominated by pyrite and arsenopyrite (Fig.
707 6a-d), which are enriched in Au, As, Ni, Cu and Pb (Fig. 10) with geometric mean

This is the peer-reviewed, final accepted version for American Mineralogist, published by the Mineralogical Society of America.
The published version is subject to change. Cite as Authors (Year) Title. American Mineralogist, in press.
DOI: https://doi.org/10.2138/am-2020-7508. http://www.minsocam.org/

Au/Ag of 3.6 (involving $py_{I-1}$ and arsenopyrite; Table 2), and contain few galena and chalcopyrite inclusions (Fig. 6a-d), whereas ore assemblage in stage II comprises pyrite containing much higher As, Pb, Cu, Sb, Zn and Ag (Fig. 11) with geometric mean Au/Ag of 0.1 (Table 2) and abundant base-metal minerals (Fig. 7c, d); and (3) sulfides in stage I have high radiogenic Pb isotope ratios and wide $\delta^{34}S$ range, whereas those in stage II have lower radiogenic Pb isotope ratios and more concentrated $\delta^{34}S$ range relative to those in stage I (Figs. 12, 13). Differences in ore assemblages (Fig. 8), trace element composition (Figs. 9-11) and S-Pb isotope data (Fig. 12) between two fluid pluses may be easily explained by two distinct fluid systems, which have been extrapolated as metamorphic and magmatic fluids by Zhang et al. (2014a) based on LA-ICP-MS trace element analysis of pyrite. However, any alteration overlap related to the fluid pluses at Chang'an is not identified by this work or previous studies in the literature (Li et at. 2011; Zhang et al. 2014). The differences noted above may also be attributed to various mineralization mechanism and changing mineralization conditions from stage I to stage II. For example, the high radiogenic Pb isotope ratios of pyrite in stage I relative to those of galena were more likely caused by the interaction of fluid and rock (or sedimentary pyrite). The more negative $\delta^{34}S$ values in sulfides in stage II may be triggered by fluid oxidation due to fracture-controlled veinlets in this stage (Fig. 7b-d; Duuring et al. 2009; Kamvong and Zaw 2009). Further deposit-scale documentation and robust geochronological studies are required to better constrain the two fluid pluses in the deposit.

## Implications

Two distinct metal-enrichment stages with distinct mineral assemblages and trace element compositions were identified in the Chang'an gold deposit. Early quartz–arsenopyrite–pyrite stage is dominated by Au mineralization with low base metals, whereas veinlet-hosted quartz–calcite–polymetallic sulfide stage is characterized by base metal mineralization with low gold. Mineral assemblages and trace elements of pyrite indicate that ore fluids in stage I are enriched in Au, As, Ni, Cu and Pb, whereas those in stage II contain As, Pb, Cu, Sb, Zn and Ag with low Au content. Replacement of syn-sedimentary pyrite with low Au content by inclusion- and Au-rich pyrite in stage I, $\delta^{34}S$ value range (10.3 ‰) of pyrite in stage I, and similar Pb isotope ratios between pyrite in stage I and syn-sedimentary pyrite indicate that reaction of external deep Au-rich fluids and syn-sedimentary pyrite is responsible for gold precipitation. Sulfur and He–Ar isotopes of sulfides and C–O isotopes of calcite in stage II indicate that ore fluids have 6–17 % mantle contribution. This study highlights that ore metals in sediment-hosted disseminated orogenic gold deposits can be sourced from both deep fluids and local wall-rock, and that fluid-pyrite interaction behaved as key control on ore precipitation.

## Acknowledgements and funding

We thank the Associate Editor Callum J. Hetherington for handling of the manuscript and crucial comments, and Prof. Robert Scott and two anonymous reviewers for

751 constructive comments. We appreciate Drs. Paul Olin, Sasha Stepanov, Lejun Zhang
752 and Xin Xiao for their suggestions and help for the LA-ICP-MS analyses of sulfides
753 and Dr. Bin Fu for his assistance for SHRIMP sulfur isotope of sulfides. This research
754 was jointly supported by the National Key Research and Development Project of China
755 (2016YFC0600307), the National Key Basic Research Development Program (973
756 Program; 2015CB452606), the Chinese Post-doctoral Innovative Talent Support
757 Program (BX20180280), China Postdoctoral Science Foundation (2018M641428) and
758 the 111 Project of the Ministry of Science and Technology (BP0719021).

## References

Ballentine, C.J., Burgess, R., and Marty, B. (2002) Tracing fluid origin, transport and interaction in the crust. Reviews in Mineralogy and Geochemistry, 47, 539–614.

Barker, S.L.L., Hickey, K.A., Cline, J.S., Dipple, G.M., Kilburn, M.R., Vaughan, J.R., and Longo, A.A. (2009) Uncloaking invisible gold: use of nanoSIMS to evaluate gold, trace elements, and sulfur isotopes in pyrite from Carlin-type gold deposits. Economic Geology, 104, 897–904.

Barker, S.L.L., and Cox, S.F. (2011) Oscillatory zoning and trace element incorporation in hydrothermal minerals: insights from calcite growth experiments. Geofluids, 11, 48–56.

Bateman, R., and Hagemann, S. (2004) Gold mineralisation throughout about 45 Ma of Archaean orogenesis: Protracted flux of gold in the Golden Mile, Yilgarn craton, Western Australia. Mineralium Deposita, 39, 536–559.

Belousov, I.A., Danyushevsky, L.V., Olin, P.H., Gilbert, S.E., and Thompson, J. (2015) STDGL3-a new calibration standard for sulphide analysis by LA-ICP-MS. Goldschmidt, Prague, Czech Republic.

Burchfiel, B.C., Chen, L., Wang, E., and Swanson, E. (2008) Preliminary investigation into the complexities of the Ailao Shan and Day Nui Con Voi shear zones of SE Yunnan and Vietnam. Investigations into the Tectonics of the Tibetan Plateau, 444, 45.

Burnard, P.G., Hu, R., Turner, G., and Bi, X.W. (1999) Mantle, crustal and atmospheric noble gases in Ailaoshan gold deposits, Yunnan Province, China. Geochimica et

781 Cosmochimica Acta, 63, 1595–1604.

782 Cai, Y., Wang, Y., Cawood, P.A., Fan, W., Liu, H., Xing, X., and Zhang, Y. (2014)
783 Neoproterozoic subduction along the Ailaoshan zone, South China:
784 Geochronological and geochemical evidence from amphibolite. Precambrian
785 Research, 245, 13–28.

786 Canfield, D.E. (2001) Isotope fractionation by natural populations of sulfate-reducing
787 bacteria. Geochimica et Cosmochimica Acta, 65, 1117–1124.

788 Canfield, D.E., and Thamdrup, B. (1994) The production of $^{34}$S-depleted sulfide during
789 bacterial disproportionation of elemental sulfur. Science, 266, 1973–1975.

790 Cao, S.Y., Liu, J.L., Leiss, B., Vollbrechr, A., Genser, J., Neubauer, F., and Zhao, C.Q.
791 (2012) Initiation of left-lateral deformation along the Ailao Shan–Red River shear
792 zone: new microstructural, textural, and geochronological constraints from the
793 Diancang Shan metamorphic massif, SW Yunnan, China. International Geology
794 Review, 54, 348–367.

795 Carter, A., Roques, D., Bristow, C., and Kinny, P. (2001) Understanding Mesozoic
796 accretion in southeast Asia: Significance of Triassic thermotectonism (Indosinian
797 orogeny) in Vietnam. Geology, 29, 211–214.

798 Cartigny, P., Harris, J.W., and Javoy, M. (1998) Eclogitic diamond formation at
799 Jwaneng: no room for a recycled component. Science, 280, 1421–1424.

800 Chang, Z.S., Large, R.R., and Maslennikov, V. (2008) Sulfur isotopes in sediment-
801 hosted orogenic gold deposits: Evidence for an early timing and a seawater sulfur
802 source. Geology, 36, 971−974.

Chen, Y., Liu, J.L., Tran, M.D., Li, Y.C., and Bing, M.M. (2010) Regional metallogenesis of the Chang'an gold ore deposit in western Yunnan Evidences from fluid inclusions and stable isotopes. Acta Geologica Sinica (English Edition), 84, 1401–1414.

Chen, Y., Yao, S., and Pan, Y. (2014) Geochemistry of lamprophyres at the Daping gold deposit, Yunnan Province, China: constraints on the timing of gold mineralization and evidence for mantle convection in the eastern Tibetan Plateau. Journal of Asian Earth Sciences, 93, 129−145.

Chinnasamy, S.S., Uken, R., Reinhardt, J., Selby, D., and Johnson, S. (2015) Pressure, temperature, and timing of mineralization of the sedimentary rock-hosted orogenic gold deposit at Klipwal, southeastern Kaapvaal Craton, South Africa. Mineralium Deposita, 50, 739–766.

Chung, S.L., Chu, M.F., Zhang, Y., Xie, Y., Lo, C.H., Lee, T.Y., Lan, C.Y., Li, X.H., Zhang, Q., and Wang, Y. (2005) Tibetan tectonic evolution inferred from spatial and temporal variations in post-collisional magmatism. Earth-Science Reviews, 68, 173–196.

Chung, S.L., Lee, T.Y., Lo, C.H., Wang, P.L., Chen, C.Y., Yem, N.T., Hoa, T.T., and Genyao, W. (1997) Intraplate extension prior to continental extrusion along the Ailao Shan-Red River shear zone. Geology, 25, 311–314.

Cline, J.S., Hofstra, A.H., Muntean, J.L., Tosdal, R.M., and Hickey, K. A. (2005) Carlin-type gold deposits in Nevada: Critical geologic characteristics and viable models. Economic Geology 100th Anniversary Volume, 451, 484.

825 Cook, N.J., Ciobanu, C.L., Meria, D., Silcock, D., and Wade, B. (2013) Arsenopyrite-
826 pyrite association in an orogenic gold ore: tracing mineralization history from
827 textures and trace elements. Economic Geology, 108, 1273–1283.
828 Crowe, D.E., and Vaughan, R.G. (1996) Characterization and use of isotopically
829 homogeneous standards for in situ laser microprobe analysis of $^{34}S/^{32}S$ ratios.
830 American Mineralogist, 81, 187–93.
831 Deditius, A.P., Reich, M., Kesler, S.E., Utsunomiya, S., Chryssoulis, S. L., Walshe, J.,
832 and Ewing, R.C. (2014) The coupled geochemistry of Au and As in pyrite from
833 hydrothermal ore deposits. Geochimica et Cosmochimica Acta, 140, 644–670.
834 Deines, P., Harris, J.W., and Gurney, J.J. (1991) The carbon isotopic composition and
835 nitrogen content of lithospheric and asthenospheric diamonds from the Jagersfontein
836 and Koffieontein kimberlites, South Africa. Geochimica et Cosmochimica Acta, 55,
837 2615–2626.
838 Deng, J., and Wang, Q. (2016) Gold mineralization in China: Metallogenic provinces,
839 deposit types and tectonic framework. Gondwana Research, 36, 219–274.
840 Deng, J., Qiu, K.F., Wang, Q.F., Goldfarb, R.J., Yang, L.Q., Zi, J.W., Geng, J.Z., and
841 Ma, Y. (2020) In-situ dating of hydrothermal monazite and implications on the
842 geodynamic controls of ore formation in the Jiaodong gold province, eastern China:
843 Economic Geology, 115: 671–685.
844 Deng, J., Wang, Q., Li, G., Hou, Z., Jiang, C., and Danyushevsky, L. (2015) Geology
845 and genesis of the giant Beiya porphyry–skarn gold deposit, northwestern Yangtze
846 Block, China. Ore Geology Reviews, 70, 457–485.

847 Deng, J., Wang, Q., Li, G., Li, C., and Wang, C. (2014) Tethys tectonic evolution and
848 its bearing on the distribution of important mineral deposits in the Sanjiang region,
849 SW China. Gondwana Research, 26, 419–437.
850 Deng, J., Wang, Q.F., Santosh, M., Liu, X.F., Liang, Y.Y., Yang, L.Q., Zhao, R., and
851 Yang, L. (2019a) Remobilization of metasomatized mantle lithosphere: a new model
852 for the Jiaodong gold province, eastern China. Mineralium Deposita, 55, 257–274.
853 Deng, J., Zhai, Y., Mo, X.X., and Wang, Q. (2019b) Temporal-spatial distribution of
854 metallic ore deposits in China and their geodynamic settings. Society of Economic
855 Geologists, 22, 103–132, doi: 10.5382/SP22.04.
856 Dunai, T.J., and Baur, H. (1995) Helium, neon and argon systematic of the European
857 subcontinental mantle: implications for its geochemical evolution. Geochim
858 Cosmochim Acta, 59, 2767–2783.
859 Duuring, P., Rowins, S.M., McKinley, B.S.M., Dickinson, J.M., Diakow, L.J., Kim, Y.S.,
860 and Creaser, R.A. (2009) Examining potential genetic links between Jurassic
861 porphyry Cu-Au ± Mo and epithermal Au ± Ag mineralization in the Toodoggone
862 district of north-central British Columbia, Canada. Mineralium Deposita, 44, 463–
863 496.
864 Evans, K.A., Phillips, G.N., and Powell, R. (2006) Rock-buffering of auriferous fluids
865 in altered rocks associated with the Golden Mile-style mineralization, Kalgoorlie
866 gold field, Western Australia. Economic Geology, 101, 805–817.
867 Faure, M., Lin, W., Chu, Y., and Lepvrier, C. (2016) Triassic tectonics of the Ailaoshan
868 belt (SW China): Early Triassic collision between the South China and Indochina

869 blocks, and Middle Triassic intracontinental shearing. Tectonophysics, 683, 27–42.
870 Fougerouse, D., Micklethwaite, S., Tomkins, A.G., Mei, Y., Kilburn, M., Guagliardo,
871 P., Fisher, L.A., Halfpenny, A., Gee, M., Paterson, D., and Howard, D.L. (2016) Gold
872 remobilisation and formation of high grade ore shoots driven by dissolution-
873 reprecipitation replacement and Ni substitution into auriferous arsenopyrite.
874 Geochim Cosmochim Acta, 178, 143–159.
875 Gao, L., Wang, Q.F., Deng, J., Zhang, S.H., and Yang, Z.Y. (2018) Relationship between
876 Orogenic Gold Mineralization and Crustal Shearing along Ailaoshan-Red River Belt,
877 Southeastern Tibetan Plateau: New Constraint from Paleomagnetism. Geochemistry,
878 Geophysics, Geosystems, 19, 2225–2242.
879 Goldfarb, R.J., Baker, T., Dube, B., Groves, D.I., Hart, C.J.R., Robert, F., and Gosselin,
880 P. (2005) Distribution, character, and genesis of gold deposits in metamorphic
881 terranes. 100th Anniversary Volume of Economic Geology, 407–450.
882 Goldfarb, R.J., and Groves, D.I. (2015). Orogenic gold: Common or evolving fluid and
883 metal sources through time. Lithos, 233, 2–26.
884 Goldfarb, R.J., Groves, D.I., and Gardoll, S. (2001) Rotund versus skinny orogens:
885 well-nourished or malnourished gold? Geology, 29, 539–542.
886 Goodwin, N.R.J., Burgess, R., Craw, D., Teagle, D.A.H., and Ballentine, C.J. (2017)
887 Noble gases fingerprint a metasedimentary fluid source in the Macraes orogenic gold
888 deposit, New Zealand. Mineralium Deposita, 52, 1–13.
889 Graupner, T., Niedermann, S., Kempe, U., Klemd, R., and Bechtel, A. (2006) Origin of
890 ore fluids in the Muruntau gold system: constraints from noble gas, carbon isotope

and halogen data: Geochimica et Cosmochimica Acta, 70, 53567–5370.

Gregory, D., Mukherjee, I., Olson, S. L., Large, R. R., Danyushevsky, L. V., Stepanov, A.S., Avila, J.N., Cliff, J., Ireland, T.R., Raiswell, R., Olin, P.H., Maslennikov, V.V., and Lyons, T.W. (2019) The formation mechanisms of sedimentary pyrite nodules determined by trace element and sulfur isotope microanalysis. Geochimica et Cosmochimica Acta, 259, 53–68.

Groves, D.I., Goldfarb, R.J., Gebre-Mariam, M., Hagemann, S.G., and Robert, F. (1998) Orogenic gold deposits: a proposed classification in the context of their crustal distribution and relationship to other gold deposit types: Ore Geology Reviews, 13, 7–27.

Groves, D.I., Goldfarb, R.J., Robert, F., and Hart C.J. (2003) Gold deposits in metamorphic belts: overview of current understanding, outstanding problems, future research, and exploration significance. Economic Geology, 98, 1–29.

Habicht, K.S., and Canfield, D.E. (1997) Sulfur isotope fractionation during bacterial sulfate reduction in organic-rich sediments. Geochimica et Cosmochimica Acta, 61, 5351–5361.

He, H.Y., Zhu, R.X., and Saxton, J. (2011) Noble gas isotopes in corundum and peridotite xenoliths from the eastern North China Craton: implication for comprehensive refertilization of lithospheric mantle. Physics of the Earth Planetary Interiors, 189, 185–191.

Hedenquist, J.W., Arribas, A., and Gonzalez-Urien, E. (2000) Exploration for epithermal gold deposits. Reviews in Economic Geology, 13, 45–77.

913 Hoefs, J. (1997) Stable Isotope Geochemistry, 3nd Edition, 201 p. Springer-Verlag,
914 Berlin.
915 Hoefs, J. (2009) Stable isotope geochemistry, 1–285 p. Springer, Heidelberg.
916 Ireland, T.R., Schram, N., Holden, P., Lanc, P., Ávila, J., Armstrong, R., Amelin, Y.,
917 Latimore, A., Corrigan, D., Clement, S., Foster, J.J., Compston, W. (2014) Charge-
918 mode electrometer measurements of S-isotopic compositions on SHRIMPSI.
919 International Journal of Mass Spectrometry, 359, 26–37.
920 Kamvong, T., and Zaw, K. (2009) The origin and evolution of skarn-forming fluids
921 from the Phu Lon deposit, northern Loei fold belt, Thailand: Evidence from fluid
922 inclusion and sulfur isotope studies. Journal of Asian Earth Sciences, 34, 624–633.
923 Kerrich, R., Goldfarb, R., Groves, D., and Garwin, S.L. (2000) The geodynamics of
924 world–class gold deposits—characteristics, space–time distribution, and origins.
925 Reviews in Economic Geology, 13, 501–544.
926 Large, R.R., Bull, S.W., and Maslennikov, V.V. (2011) A carbonaceous sedimentary
927 source rock model for Carlin-type and orogenic gold deposits. Economic Geology,
928 106, 331–358.
929 Large, R.R., Danyushevsky, L., Hollitt, C., Maslennikov, V., Meffre, S., Gilbert, S., Bull,
930 S., Scott, R., Emsbo, P., Thomas, H., Singh, B., and Foster, J. (2009) Gold and trace
931 element zonation in pyrite using a laser imaging technique: Implications for the
932 timing of gold in orogenic and Carlin-style sediment-hosted gold deposits. Economic
933 Geology, 104, 635–668.
934 Large, R.R., Halpin, J.A., Danyushevsky, L.V., Maslennikov, V.V., Bull, S.W., Long,

J.A., Gregory, D.D., Lounejeva, E., Lyons, T.W., Sack, P.J., and others. (2014) Trace element content of sedimentary pyrite as a new proxy for deeptime ocean-atmosphere evolution. Earth and Planetary Science Letters, 389, 209–220.

Large, R.R., Maslennikov, V.V., Robert, F., Danyushevsky, L.V., and Chang, Z. (2007) Multistage sedimentary and metamorphic origin of pyrite and gold in the giant Sukhoi Log deposit, Lena gold province, Russia. Economic Geology, 102, 1233–1267.

Large, R.R., Meffre, S., Burnett, R., Guy, B., Bull, S., Gilbert, S., Goemann, K., and Danyushevsky, L. (2013) Evidence for an intrabasinal source and multiple concentration processes in the formation of the Carbon Leader Reef, Witwatersrand Supergroup, South Africa. Economic Geology, 108, 1215–1241.

Lawrence D.M., Treloar P.J., Rankin A.H., Boyce, A., and Harbidge, P. (2013) A fluid inclusion and stable isotope study at the Loulo mining district, Mali, West Africa: implications for multifluid sources in the generation of orogenic gold deposits. Economic Geology, 108, 229–257.

Leloup, P.H., Lacassin, R., Tapponnier, P., Schärer, U., Zhong, D., Liu, X., Zhang, L., Ji, S., and Trinh, P.T. (1995) The Ailao Shan-Red river shear zone (Yunnan, China), tertiary transform boundary of Indochina. Tectonophysics, 251, 3–84.

Li, H., Wang, Q., Deng, J., Yang, L., Dong, C., and Yu, H. (2019a) Alteration and mineralization styles of the orogenic disseminated Zhenyuan gold deposit, southeastern Tibet: Contrast with carlin gold deposit. Geoscience Frontiers, 10, 1849–1862.

957 Li, H., Wang, Q., Groves, D. I., Deng, J., Dong, C., Wang, X., and Yang, L. (2019b)
958 Alteration of Eocene lamprophyres in the Zhenyuan orogenic gold deposit, Yunnan
959 Province, China: Composition and evolution of ore fluids. Ore Geology Reviews,
960 107, 1068–1083.
961 Li, S.H., Zhang, J., Deng, J., Wang, H., Liu, J.T., and Zhao, K. (2011) The
962 characteristics of oreforming fluid and genetic type of the Chang'an gold deposit in
963 Southern Ailaoshan metallogenic belt. Acta Petrologica Sinica, 27, 3777–3786 (in
964 Chinese with English abstract).
965 Li, X., Wang, C., Hua, R., and Wei, X. (2010) Fluid origin and structural enhancement
966 during mineralization of the Jinshan orogenic gold deposit, South China. Mineralium
967 Deposita, 45, 583–597.
968 Li, Z.K., Li, J.W., Cooke, D.R., Danyushevsky, L., Zhang, L., O'Brien, H., Lahaye, Y.,
969 Zhang, W., and Xu, H.J. (2016) Textures, trace elements, and Pb isotopes of sulfides
970 from the Haopinggou vein deposit, southern North China Craton: implications for
971 discrete Au and Ag–Pb–Zn mineralization. Contributions to Mineralogy and
972 Petrology, 171, 99.
973 Liu, F., Wang, F., Liu, P., and Liu, C. (2013) Multiple metamorphic events revealed by
974 zircons from the Diancang Shan–Ailao Shan metamorphic complex, southeastern
975 Tibetan Plateau. Gondwana Research, 24, 429–450.
976 Liu, H.C., Wang, Y.J., Cawood, P.A., Fan, W.M., Cai, Y.F., and Xing, X.W. (2015a)
977 Record of Tethyan Ocean closure and Indosinian collision along the Ailaoshan suture
978 zone (SW China). Gondwana Research, 27, 1292–1306.

979 Liu, J., Chen, X., Wu, W., Tang, Y., Tran, M.D., Nguyen, Q.L., Zhang, Z.C., and Zhao,
980 Z. (2015b) New tectono-geochronological constraints on timing of shearing along
981 the Ailao Shan-Red River shear zone: implications for genesis of Ailao Shan gold
982 mineralization. Journal of Asian Earth Sciences, 103, 70–86.
983 Lu, Y.J., Kerrich, R., Mccuaig, T.C., Li, Z.X., Hart, C.J., Cawood, P.A., Hou, Z.Q.,
984 Bagas, L., Cliff, J., Belousova, E.A., and Tang, S.H. (2013) Geochemical, Sr–Nd–
985 Pb, and zircon Hf–O isotopic compositions of Eocene–Oligocene shoshonitic and
986 potassic adakite-like felsic intrusions in western Yunnan, SW China: petrogenesis
987 and tectonic implications. Journal of Petrology, 54, 1309–1348.
988 Mao, J.W., Li, Y., Goldfarb, R., He, Y., and Zaw, K. (2003) Fluid inclusions and noble
989 gas studies of the Dongping gold deposit, Heibei Province, China: a mantle
990 connection for mineralization. Economic Geology, 98, 517–534.
991 Meffre, S., Large, R.R., Scott, R., Woodhead, J., Chang, A., Gilbert, S.E.,
992 Danyushevsky, L.V., Maslennikov, V., and Hergt, J.M. (2008) Age and pyrite Pb-
993 isotopic composition of the giant Sukhoi Log sediment-hosted gold deposit, Russia.
994 Geochimica et Cosmochimica Acta, 72, 2377–2391.
995 Mukherjee, I., Large, R.R., Bull, S., Gregory, D.G., Stepanov, A.S., Ávila, J., Ireland,
996 T.R., and Corkrey, R. (2019) Pyrite trace-element and sulfur isotope geochemistry of
997 paleo-mesoproterozoic McArthur Basin: Proxy for oxidative weathering. American
998 Mineralogist, 104, 1256–1272.
999 Ohmoto H., and Rye R.O. (1979) Isotopes of sulfur and carbon. In H.L. Barnes, Eds.,
1000 Geochemistry of hydrothermal ore deposits, 509–567. Wiley, New York.

1001 Ohmoto, H. (1972) Systematics of sulfur and carbon isotopes in hydrothermal ore
1002 deposits. Economic Geology, 67, 551–578.
1003 Ozima, M., and Podosek, F.A. (2002) Noble gas geochemistry, 286 p. Cambridge
1004 University Press, Cambridge.
1005 Peterson, E., and Mavrogenes, J. (2014) Linking high-grade gold mineralization to
1006 earthquake-induced fault-valve processes in the Porgera gold deposit, Papua New
1007 Guinea. Geology, 42, 383–386.
1008 Pitcairn, I.K., Teagle, D.A.H., Craw, D., Olivo, G.R., Kerrich, R., and Brewer, T.S.
1009 (2006) Sources of metals and fluids in orogenic gold deposits: Insights from the
1010 Otago and Alpine Schists, New Zealand. Economic Geology, 101, 1525–1546.
1011 Ray, J.S., Ramesh, R., and Pande, K. (1999) Carbon isotopes in Kerguelen plume-
1012 derived carbonatites: evidence for recycled inorganic carbon. Earth and Planetary
1013 Science Letters, 170, 205–214.
1014 Reich, M., Kesler, S.E., Utsunomiya, S., Palenik, C.S., Chryssoulis, S.L., and Ewing,
1015 R. (2005) Solubility of gold in arsenian pyrite. Geochimica et Cosmochimica Acta,
1016 69, 2781–2796.
1017 Ridley, J.R., and Diamond, L.W. (2000) Fluid chemistry of orogenic lode gold deposits
1018 and implications for genetic models. Reviews in Economic Geology, 13, 141–162.
1019 Sack, R.O., Lynch, J., and Foit, F. (2003) Fahlore as a petrogenetic indicator: Keno Hill
1020 Ag–Pb–Zn district, Yukon, Canada. Mineralogical magazine, 67, 1023–1038.
1021 Schärer, U., Zhang, L.S., and Tapponnier, P. (1994) Duration of strike–slip movements
1022 in large shear zones: the Red River belt, China. Earth and Planetary Science Letters,

126, 379–397.

Seward, T.M. (1991) The hydrothermal geochemistry of gold. In R.P. Foster, Eds., Gold metallogeny and exploration, 37–62 p, Glasgow, Blackie.

Sibson, R. H., and Scott, J. (1998) Stress/fault controls on the containment and release of overpressured fluids: Examples from gold-quartz vein systems in Juneau, Alaska; Victoria, Australia and Otago, New Zealand. Ore Geology Reviews, 13, 293–306.

Sillitoe, R.H. (1997) Characteristics and controls of the largest porphyry copper-gold and epithermal gold deposits in the circum-Pacific region. Australian Journal of Earth Sciences, 44, 373–388.

Steadman, J.A., and Large, R.R. (2016) Synsedimentary, diagenetic, and metamorphic pyrite, pyrrhotite, and marcasite at the Homestake BIF-hosted gold deposit, South Dakota, USA: insights on Au-As ore genesis from textural and LA-ICP-MS trace element studies. Economic Geology, 111, 1731–1752.

Steadman, J.A., Large, R.R., Meffre, S., and Bull, S.W. (2013) Age, origin and significance of nodular sulfides in 2680 Ma carbonaceous black shale of the Eastern Goldfields Superterrane, Yilgarn craton, Western Australia. Precambrian Research, 230, 227–247.

Stefánsson, A., and Seward, T.M. (2004) Gold (I) complexing in aqueous sulphide solutions to 500°C at 500 bar. Geochimica et Cosmochimica Acta, 68, 4121–4143.

Strauss, H. (2006) Anoxia through time: Reviews of Geophysics, 33, 241−265.

Stepanov, A.S. (2019) Arsenic evolution as a tool for understanding formation of pyritic gold ores: COMMENT. Geology, 47, e491−e491.

1045 Sun, X.M., Zhang, Y., Xiong, D., Sun, W., Shi, G.Y., Zhai, W., and Wang, S.W. (2009)
1046 Crust and mantle contributions to gold-forming process at the Daping deposit,
1047 Ailaoshan gold belt, Yunnan, China. Ore Geology Reviews, 36, 235−249.
1048 Tanner, D., Henley, R.W., Mavrogenes, J.A., and Holden, P. (2016) Sulfur isotope and
1049 trace element systematics of zoned pyrite crystals from the El Indio Au–Cu–Ag
1050 deposit, Chile. Contributions to Mineralogy and Petrology, 171, 33.
1051 Tapponnier, P., Lacassin, R., Leloup, P.H., Schärer, U., Zhong, D.L., Wu, H.W., Liu,
1052 X.H., Ji, S.C., Zhang, L.S., and Zhong, J.Y. (1990) The Ailao Shan/Red River
1053 metamorphic belt: tertiary left–lateral shear between Indochina and South China.
1054 Nature, 343, 431.
1055 Thomas, H.V., Large, R.R., Bull, S.W., Maslennikov, V., Berry, R.F., Fraser, R., Froud,
1056 S., and Moye, R. (2011) Pyrite and pyrrhotite textures and composition in sediments,
1057 laminated quartz veins, and reefs at Bendigo gold mine, Australia: Insights for ore
1058 genesis. Economic Geology, 106, 1–31.
1059 Tian, G., Zhang, C.Q., Peng, H.J., Zhou, Y.M., Li, J.R., Zhang, X.P., and Hu, M.Y. (2014)
1060 Petrogenesis and geodynamic setting of the Chang'an gold deposit in southern
1061 Ailaoshan metallogenic belt. Acta Petrologica Sinica, 30, 125–138 (in Chinese with
1062 English abstract).
1063 Tolstikhin, I.N. (1978) A review: some recent advances in isotope geochemistry of light
1064 noble gases. In E.C. Jr. Alexander, M. Ozima, Eds., Terrestrial noble gases, 33–62 p.
1065 Japan Sci Press, Tokyo.
1066 Tomkins, A.G. (2010) Windows of metamorphic sulfur liberation in the crust:

1067 Implications for gold deposit genesis. Geochimica et Cosmochimica Acta, 74, 3246–
1068 3259.
1069 Treloar, P.J., Lawrence, D.M., Senghor, D., Boyce, A., and Harbidge, P. (2015) The
1070 Massawa gold deposit, Eastern Senegal, West Africa: an orogenic gold deposit
1071 sourced from magmatically derived fluids? Geological Society, London, Special
1072 Publications, 393, 135–160.
1073 Velasquez, G., Beziat D., Salvi, S., Siebenaller, L., Borisova, A.Y., Pokrovski, G.B.,
1074 and de Parseval, P. (2014) Formation and deformation of pyrite and implications for
1075 gold mineralization in the El Callao District, Venezuela. Economic Geology, 109,
1076 457–486.
1077 Voute, F., Hagemann, S. G., Evans, N. J., and Villanes, C. (2019) Sulfur isotopes, trace
1078 element, and textural analyses of pyrite, arsenopyrite and base metal sulfides
1079 associated with gold mineralization in the Pataz-Parcoy district, Peru: implication for
1080 paragenesis, fluid source, and gold deposition mechanisms. Mineralium Deposita, 54,
1081 1077–1100.
1082 Wang, D.H., Qu, W.J., Li, Z.W., Ying, H.L., and Chen, Y.C. (2005) The ore-forming
1083 centralism time of porphyry copper–molybdenum deposit in Jinsha River–Red River
1084 ore-forming belt: Re–Os isotope dating. Science in China (Ser D-Earth Science), 48,
1085 192–198.
1086 Wang, J., Qi, L., Yin, A., and Xie, G. (2001) Emplacement age and PGE geochemistry
1087 of lamprophyres in the Laowangzhai gold deposit, Yunnan, SW China. Science in
1088 China Series D: Earth Sciences, 44, 146–154.

1089 Wang, Q.F., and Groves, D.I., (2018) Carlin-style gold deposits, Youjiang Basin, China:
1090 tectono-thermal and structural analogues of the Carlin-type gold deposits, Nevada,
1091 USA. Mineralium Deposita, 53, 909–918.
1092 Wang, Q.F., Deng, J., Li, C.S., Li, G.J., Yu, L., and Qiao, L. (2014) The boundary
1093 between the Simao and Yangtze blocks and their locations in Gondwana and Rodinia:
1094 constraints from detrital and inherited zircons. Gondwana Research, 26, 438–448.
1095 Wang, Q.F., Deng, J., Weng, W.J., Li, H.J., Wang, X., and Li, G.J. (2020) Cenozoic
1096 orogenic gold system in Tibet. Acta Petrologica Sinica, 36, 1315–1353 (in Chinese
1097 with English abstract).
1098 Wang, Q.F., Groves, D.I., Deng, J., Li, H.J., Yang, L., and Dong, C.Y. (2019) Evolution
1099 of the Miocene Ailaoshan orogenic gold deposits, southeastern Tibet, during a
1100 complex tectonic history of lithosphere-crust interaction. Mineralium Deposita,
1101 doi.org/10.1007/s00126-019-00922-3.
1102 Wang, Y. (2008) The ore-forming model and geological characteristics of Chang'an
1103 gold deposit in Jinping, Yunnan. Beijing: Chinese Academy of Geological Sciences,
1104 178.
1105 Wang, Y., Zhang, B., Schoenbohm, L.M., Zhang, J., Zhou, R., Hou, J., and Ai, S. (2016)
1106 Late Cenozoic tectonic evolution of the Ailao Shan–Red River fault (SE Tibet):
1107 Implications for kinematic change during plateau growth. Tectonics, 35, 1969–1988.
1108 Weatherley, D.K., and Henley, R.W. (2013) Flash vaporization during earth quakes
1109 evidenced by gold deposits. Nature Geoscience, 6, 294–298.
1110 Wilde, A.R., Layer, P., Mernagh, T., and Foster, J. (2001) The giant Muruntau gold

deposit: geologic, geochronologic, and fluid inclusion constraints on ore genesis. Economic Geology, 96, 633–644.

Williams-Jones, A.E., Bowell, R.J., and Migdisov, A.A. (2009) Gold in solution. Elements, 5, 281–287.

Woodhead, J., Hergt, J., Meffre, S., Large, R.R., Danyushevsky, L., and Gilbert, S. (2009) In situ Pb-isotope analysis of pyrite by laser ablation (multi-collector and quadrupole) ICPMS. Chemical Geology, 262, 344–354.

Wu, Y.F., Fougerouse, D., Evans, K., Reddy, S.M., Saxey, D.W., Guagliardo, P., and Li, J.W. (2019) Gold, arsenic, and copper zoning in pyrite: A record of fluid chemistry and growth kinetics. Geology, 47, 641–644.

Yang, L., Wang, Q.F., Wang, Y., and Li, G.J. (2018) Proto- to paleo-Tethyan evolution of the eastern margin of Simao block. Gondwana Research, 62, 61–74.

Yang, L.Q., Deng, J., Wang, Z.L., Guo, L.N., Li, R.H., Groves, D.I., Danyushevsky, L.V., Zhang, C., Zheng, X.L., and Zhao, H. (2016) Relationships between gold and pyrite at the Xincheng gold deposit, Jiaodong Peninsula, China: Implications for gold source and deposition in a brittle epizonal environment. Economic Geology, 111, 105–126.

Yang, L.Q., Deng, J., Zhao, K., and Liu, J.T. (2011) Tectono-thermochronology and gold mineralization events of orogenic gold deposits in Ailaoshan orogenic belt, Southwest China: geochronological constraints. Acta Petrologica Sinica, 27, 2519–2532 (in Chinese with English abstract).

Yang, L.Q., Liu, J.T., Zhang, C., Wang, Q.F., Ge, L.S., Wang, Z.L., Zhang, J., and Gong,

Q.J. (2010) Superimposed orogenesis and metallogenesis: an example from the orogenic gold deposits in Ailaoshan gold belt, Southwest China. Acta Petrologica Sinica, 26, 1723–1739 (in Chinese with English abstract).

YNGMR (Yunnan Bureau of Geology and Mineral Resources) (1990) Regional Geology of Yunnan Province, 45–201 p. Geological Publishing House, Beijing. (in Chinese).

Yin, A., and Harrison, T. M. (2000) Geologic evolution of the Himalayan-Tibetan orogen. Annual Review of Earth and Planetary Sciences, 28, 211–280.

Zartman, R.E., and Doe, B.R. (1981) Plumbotectonics—the model. Tectonophysics, 75, 135–162.

Zhang, C., Qi, X.X., Tang, G.Z., Zhao, Y.H., and Ji, F.B. (2014b) Geochemistry and zircon U–Pb dating for the alkaline porphyries and its constraint on the mineralization in Chang'an Cu–Mo–Au ore concentration region, Ailaoshan orogenic belt, western Yunnan. Acta Petrologica Sinica, 30, 2204–2216.

Zhang, J., Deng, J., Chen, H.Y., Yang, L.Q., Cooke, D., and Danyushevsky, L. (2014a) LA-ICP-MS trace element analysis of pyrite from the Chang'an gold deposit, Sanjiang region, China: implication for ore-forming process. Gondwana Research, 26, 557–575.

Zhang, J., Wang, H., Li, S., and Li, T. (2017). Paleogene magmatism and gold metallogeny of the Jinping terrane in the Ailaoshan ore belt, Sanjiang Tethyan Orogen (SW China): Geology, deposit type and tectonic setting. Ore Geology Reviews, 91, 620–637.

Zhang, L.S., and Schärer, U. (1999) Age and origin of magmatism along the Cenozoic Red River shear belt, China. Contributions to Mineralogy and Petrology, 134, 67–85.

Zhao, H.S., Wang, Q.F., Groves, D.I., and Deng, J. (2018) A rare Phanerozoic amphibolite-hosted gold deposit at Danba, Yangtze Craton, China: significance to fluid and metal sources for orogenic gold systems. Mineralium Deposita, 54, 133–152.

Zhou, C., Wei, C., and Li, C. (1998) The igneous rock suite of lower Sinian system along the southwest margin of Yangtse block. Acta Mineralogica Sinica, 18, 401–410.

Zhu, X.P., Mo, X.X., White, N., Zhang, B., Sun, M.X., Wang, S.X., Zhao, S.L., and Yang, Y. (2009) Geology and Metallogenetic Setting of the Habo Porphyry Cu (Mo-Au) Deposit, Yunnan. Acta Geologica Sinica, 83, 1915–1928 (in Chinese with English abstract).

## Figure Captions

**Figure 1.** (**a**) Generalized map showing major tectonic structures developed during the collision between India and Eurasia and the geographic location of the Ailaoshan orogenic belt (revised from Tapponnier et al. (1990)). Red dashed line represents part of current China National boundary. (**b**) Geological map of the Ailaoshan gold belt showing the distribution of high- and low-grade metamorphic belts. The location of the Chang'an gold deposit in the low-grade Jinping terrane is indicated (revised from Wang et al. (2014)).

**Figure 2.** (**a**) Geological map of the Chang'an gold deposit, showing the major lithologic units, widespread wall-rock alteration halo and gold orebodies (revised from Yunnan Gold Mining Co. Ltd, unpublished report, 2015). (**b**) Cross-section of the Chang'an gold deposit, showing lithologic units, wall-rock alteration, and geometry of ore bodies. Modified from the unpublished internal geological map of Yunnan Gold Mining Co. Ltd. Two colors in a legend (turbidite, dolostone, syenite or lamprophyre) represent unaltered (to the left) and altered (to the right) rock.

**Figure 3.** Photograph of open mining pit, showing distribution of lithologic units, structures, and sample locations as well as contour map of Au grade at 1580 m level.

**Figure 4.** Photographs of structural features, crosscutting relationship and mineralization styles. (**a**) Sedimentary pyrites ($py_s$; outlined by dashed ellipses) in the

Ordovician strata. (**b**) A syenite dike cutting an earlier lamprophyre. (**c**) Core of the Chang'an fault composed of several secondary faults in the northern part of the open pit. (**d**) Striations and steps in the fault planes of the Chang'an fault, showing a sense of sinistral-reverse movement. (**e**) An EW-trending quartz-calcite-polymetallic sulfide veinlet in the Ordovician sandstone. (**f**) A NS-trending quartz-calcite-polymetallic sulfide veinlet in the syenite. (**g**) NW-trending quartz-calcite veinlets in the Ordovician sandstone.

**Figure 5.** Photomicrographs (cross-polarized light: a-c and e; BSE: d; plane-polarized light: f) of different rocks showing the alteration characteristics in the Chang'an gold deposit. (**a**) Quartz-, sericite-, and pyrite ($py_s$ and $py_{I\text{-}1}$)-altered sandstone. (**b**) Quartz-, sericite-, pyrite ($py_{I\text{-}1}$)- and arsenopyrite-altered sandstone. (**c**) Quartz-, sericite-, and pyrite ($py_{I\text{-}Sy}$)-altered syenite. (**d**) Quartz-, and ankerite-, and sphalerite-altered syenite. The ankerite and sphalerite, together with the apatite and rutile, are distributed along the cleavage of biotite. White dashed lines mark outlines of biotite. (**e**) Calcite- and pyrite ($py_{II\text{-}1}$)-altered sandstone, showing a cogenetic calcite and $py_{II\text{-}1}$. (**f**) Quartz-, sericite-, pyrite ($py_s$ and $py_{I\text{-}1}$)- and calcite-altered sandstone. The calcite cuts the quartz, sericite and pyrite ($py_s$ and $py_{I\text{-}1}$). Abbreviation: Ank=ankerite, Ap=apatite, Apy= arsenopyrite, Bt=biotite, Cal=calcite, Py=pyrite ($py_s$, $py_{I\text{-}1}$, $py_{I\text{-}Sy}$ and $py_{II\text{-}1}$ represent different generations of pyrite), Qtz=quartz, Rut=rutile, Ser=sericite, Sp=sphalerite.

**Figure 6.** BSE images showing the mineralogy, pyrite texture and paragenesis in pre-

ore and hydrothermal stage I. Also shown are the locations of representative spot analyses for sulfur isotopes (red) and Au concentration (pink) results of selected sulfide grains. (**a**) Subhedral $py_s$ overlapped by $py_{I-1}$ containing inclusions of arsenopyrite. (**b**) Subhedral $py_s$ overgrown by $py_{I-1}$ with galena inclusions. Apertures in $py_s$ are filled by quartz and calcite. (**c**) Subhedral $py_s$ overgrown by oscillatory zoning $py_{I-1}$ with arsenopyrite inclusions along the contact between $py_s$ and $py_{I-1}$. (**d**) Corrosive $py_s$ with irregular contact boundary overgrown by $py_{I-1}$, which in turn is rimmed by $py_{I-2}$. Abbreviation: Apy= arsenopyrite, Cal=calcite, Py=pyrite ($py_s$, $py_{I-1}$ and $py_{I-2}$ represent different generations of pyrite), Qtz=quartz.

**Figure 7.** BSE images showing the mineralogy, pyrite texture and paragenesis of hydrothermal stages I and II. Also shown are the locations of representative spot analyses for sulfur isotopes (red) and Au concentration (pink) results of selected sulfide grains. (**a**) Unzoned $py_{I-Sy}$ with porous texture filled by quartz, galena and arsenopyrite in stage I in the syenite. (**b**) $Py_{I-1}$ with oscillatory zoning overgrown by $py_{I-2}$ in stage I, which is cut by subhedral to anhedral $py_{II-1}$ (with porous texture filled by galena) overgrown by euhedral $py_{II-2}$ in stage II. (**c**) Subhedral to euhedral $py_{II-1}$ overgrown by $py_{II-2}$ with cogenetic Ga in stage II. (**d**) A cogenetic mineral assemblage of $py_{II-2}$, galena and arsenopyrite, chalcopyrite, tetrahedrite, proustite, sphalerite in stage II. Abbreviation: Apy= arsenopyrite, Ccp=chalcopyrite, Ga=galena, Pr=proustite, Py=pyrite ($py_{I-1}$, $py_{I-Sy}$, $py_{I-2}$, $py_{II-1}$ and $py_{II-2}$ represent different generations of pyrite), Qtz=quartz, Sp=sphalerite, Tet= tetrahedrite.

**Figure 8.** Interpreted paragenetic sequence of pre-ore and ore-related minerals in the Chang'an gold deposit. Small yellow cycles indicate the phase contains invisible gold.

**Figure 9.** LA-ICP-MS images of trace elements (ppm) in pyrite from sample CA33. The pyrite core ($py_S$) contains minor electrum inclusions and contains up to ~1 wt% Co and Ni in solid solution. The pyrite inner zone ($py_{I-1}$) has higher Au, As, Ag, Co, Ni, Pb, Sb and Cu concentrations relative to $py_S$ and the rimming pyrite ($py_{I-2}$), which has low As, Co, Ni, Pb and Au contents. See text for more explanation of pyrite generations and their compositions.

**Figure 10.** LA-ICP-MS images of trace elements (ppm) in pyrite from sample CA38. Pyrite inner zone ($py_{II-1}$) is enriched in Au, As, Ag, Co, Ni, Pb, Sb and Cu. $Py_{II-1}$ contains Au-Ag-Sb-Cu inclusions, possible suggestive of Au-bearing polybasite. Pyrite outer zone ($py_{II-2}$) shows As-Co-Ni enrichment and zonation but depletion in Au. See text for more explanation of pyrite generations and their compositions. Red lines represent inferred cracks in pyrite.

**Figure 11.** Interelement correlations for pyrites of different generations and arsenopyrite from samples CA01, CA20, CA25, CA29, CA33, CA36 and CA38. (**a**) Au-As. Black solid line in Figure a is Au saturation line defined by Reich et al. (2005) and red dashed line is preferred Au saturation line of arsenian pyrite from the Chang'an

gold deposit. (**b**) Au-Cu. (**c**) Au-Ag. (**d**) Au-Sb. (**e**) Co-Ni. (**f**) Pb-Ag.

**Figure 12.** Sulfur isotope composition of different generations of pyrites and arsenopyrites in the Chang'an gold deposit. Variation curves of $\delta^{34}S$ values of pyrites in the sedimentary rock-hosted orogenic gold deposits and sulfate seawater through time are based on Chang et al. (2008). Dashed line marks the $\delta^{34}S$ value of 0 ‰ and yellow shadow area represents the $\delta^{34}S$ range of sulfides in hydrothermal stages I and II.

**Figure 13.** *In situ* Pb isotope of different generations of pyrite and galena in the Chang'an gold deposit. The field for western Yunnan volcanics is from Zhou et al. (1998). The field for western Yunnan potassic mafic rocks is from Lu et al. (20013). The field for leucogranite within the Ailao Shan-Red River shear zone (ASRR) in western Yunnan is from Zhang and Schärer (1999).

**Figure 14.** (**a**) R/Ra vs. $^{40}Ar^*/^4He$ diagram of fluid inclusions in composites of $py_{II\text{-}1}$-$py_{II\text{-}2}$ in the Chang'an gold deposit, in comparison to typical crustal and mantle reservoirs (Ballentine et al. 2002; Ozima and Podosek 2002) as well as those in the Murantau, Macreas, Zhenyuan, Daping and Dongping gold deposits (Burnard et al. 1999; Mao et al. 2003; Graupner et al. 2006; Sun et al. 2009; Goodwin et al. 2017). The $^{40}Ar^*$ is the $^{40}Ar$ content corrected for atmospheric contribution. (**b**) $\delta^{13}C_{PDB}$–$\delta^{18}O_{PDB}$ diagram of calcites in hydrothermal stages II and III. Fields for sedimentary carbonate

and sedimentary organic carbon are from Hoefs (2009) and field for mantle is from Ray et al. (1999).

**Supplementary Materials**

**Table S1.** Laser Ablation-Inductively Coupled Plasma-Mass Spectrometry (LA-ICP-MS) analyses of pyrite and arsenopyrite from the Chang'an gold deposit.

**Table S2**. In situ sulfur isotope composition of different sulfide types from the Chang'an gold deposit.

**Table S3.** In situ Pb isotopic composition of pyrite and galena from Chang'an gold deposit.

**Table S4.** He-Ar isotopic composition of composites of $Py_{II-1}$-$Py_{II-2}$ in hydrothermal stage II in the Chang'an gold deposit.

**Table S5.** C-O isotopic composition of calcites in hydrothermal stages II and III in the Chang'an gold deposit

**Figure S1.** LA-ICP-MS count outputs for a composite of (**a**) $py_s$-$py_{I-1}$ from sample CA20 and (**b**) $py_{II-1}$-$py_{II-2}$ from sample CA38. Insets show the analyzed pyrites and paths of the laser analysis (arrows indicate the direction of ablation). Note that the $py_s$

is lower Au, As and Pb contents, compared to the surrounding $py_{I-1}$, which is enriched in Au and As compared to $py_{II-1}$ and $py_{II-2}$. The pattern of analyzed $py_{II-1}$ and $py_{II-2}$ indicates micro-inclusions of galena and free gold.

**Figure S2.** LA-ICP-MS images of trace elements (ppm) in pyrite from sample CA20. Core of the pyrite ($py_s$) contains Au, As, Ag, Co, Ni, Pb, Sb and Cu. Rim of the pyrite ($py_{I-1}$) is more enriched in these elements. See text for more explanation of pyrite generations and their compositions.

**Figure S3.** LA-ICP-MS images of trace elements (ppm) in pyrite from sample CA25. Pyrite core ($py_s$) has higher Co, Ni and Pb concentrations than the rimming pyrite ($py_{I-1}$), which has higher Au, As, Ag, Co, Ni, Pb, Sb and Cu contents. See text for more explanation of pyrite generations and their compositions.

**Figure S4.** LA-ICP-MS images of trace elements (ppm) in pyrite ($py_{I-Sy}$) from sample CA29. $Py_{I-Sy}$ has high As, Ni and Co contents with inclusions of chalcopyrite, galena and sphalerite.

This is the peer-reviewed, final accepted version for American Mineralogist, published by the Mineralogical Society of America.
The published version is subject to change. Cite as Authors (Year) Title. American Mineralogist, in press.
DOI: https://doi.org/10.2138/am-2020-7508. http://www.minsocam.org/

1317 Table 1. Summary of common textures and pyrite classification for the Chang'an gold deposit

| Pyrite | Timing | Host rock | Texture | Co-genetic minerals | Evidence for timing |
|---|---|---|---|---|---|
| $Py_S$ | Synsedimentary/ diagenetic | Turbidite | Bedding-parallel nodule; corroded structure | Detrital quartz, Fe-dolomite, apatite | Bedding parallel; nodal texture (Fig. 4a); overgrown by $py_{I-1}$ (Fig. 6a-d) |
| $Py_{I-1}$ | Hydrothermal stage I | Turbidite | Euhedral-subhedral; oscillatory zoning structure; inclusion-rich | Fine-grained quartz, arsenopyrite, galena, chalcopyrite and electrum | Overgrow $py_S$ and overgrown by $py_{I-2}$ (Fig. 6a-d); crosscut by $py_{II-1}$ and $py_{II-2}$ (Fig. 7b) |
| $Py_{I-2}$ | Hydrothermal stage I | Turbidite | Euhedral to subhedral; outer thin rim; inclusion-free | No or rarely | Overgrow $py_{I-1}$ (Fig. 6a, d); crosscut by $py_{II-1}$ and $py_{II-2}$ (Fig. 7b) |
| $Py_{I-Sy}$ | Hydrothermal stage I | Syenite | Euhedral to subhedral; disseminated | Fine-grained quartz, arsenopyrite, galena | Similar mineral assemblage to $py_{I-1}$ (Fig. 7a) |
| $Py_{II-1}$ | Hydrothermal stage II | Turbidite | Subhedral; porous textures; inclusion-rich | Abundant fine-grained inclusions of galena, sphalerite, and tetrahedrite | Crosscut $py_{I-1}$ and $py_{I-2}$ (Fig. 7b) |
| $Py_{II-2}$ | Hydrothermal stage II | Turbidite | Euhedral | Euhedral galena, chalcopyrite, sphalerite, tetrahedrite and proustite | Crosscut or overgrow $py_{II-1}$ (Fig. 7b, c) |

1318 Explanation of nomenclatures: "Py" represents pyrite; "S" and "Sy" represent sedimentary rock and syenite, respectively; "I" and "II" donate hydrothermal stages I and II,
1319 respectively; "-1" and "-2" represent the first and second generations of pyrite. For example, $py_S$ represent sedimentary pyrite, $py_{I-1}$ donates the first generation of pyrite formed
1320 in hydrothermal stage I, and $py_{I-Sy}$ represent stage-I pyrite in syenite.

1321

1322

1323 **Table 2.** Summarized Laser Ablation-Inductively Coupled Plasma-Mass Spectrometry (LA-ICP-MS) analyses of pyrite and arsenopyrite from

1324 the Chang'an gold deposit

| | Co | Ni | Cu | Zn | As | Se | Mo | Ag | Sb | Te | Au | Tl | Pb | Bi | Au/Ag |
|---|---|---|---|---|---|---|---|---|---|---|---|---|---|---|---|
| $Py_s$ (n=14) | | | | | | | | | | | | | | | |
| Min | 7.3 | 8.7 | 1.4 | 1.1 | 2.3 | 4.1 | b.d.l | 0.1 | 0.1 | b.d.l | 0.0 | 0.0 | 14.2 | b.d.l | 0.0 |
| Max | 204.1 | 358.5 | 30.0 | 12.1 | 10371 | 10.9 | 264.0 | 2.3 | 33.2 | 10.3 | 0.5 | 43.7 | 196.0 | 100.8 | 1.1 |
| Mean | 23.4 | 59.8 | 13.0 | 4.1 | 620.8 | 8.3 | 54.4 | 0.4 | 4.8 | 3.3 | 0.1 | 4.1 | 61.6 | 0.7 | 0.1 |
| S.D. | 51.5 | 105.2 | 8.9 | 2.8 | 3569.2 | 2.2 | 79.4 | 79.4 | 11.5 | 2.9 | 0.2 | 14.9 | 42.9 | 30.2 | 0.3 |
| $Py_{I\text{-}1}$ (n=23) | | | | | | | | | | | | | | | |
| Min | 2.7 | 19.8 | 7.4 | b.d.l | 1247 | b.d.l | b.d.l | b.d.l | 2.2 | b.d.l | 0.6 | 0.1 | 19.0 | 0.0 | 0.0 |
| Max | 767.5 | 599.1 | 2242.7 | 59.4 | 44583 | 16.1 | 282.7 | 74.6 | 102.7 | 3.9 | 227.1 | 19.5 | 803.5 | 11.6 | 85.6 |
| Mean | 79.8 | 248.1 | 139.9 | 8.4 | 8931 | 9.6 | 47.6 | 8.2 | 26.2 | 0.9 | 8.9 | 2.5 | 120.0 | 1.3 | 1.2 |
| S.D. | 225.9 | 192.9 | 472.9 | 14.6 | 13421 | 3.6 | 92.6 | 23.9 | 28.9 | 1.3 | 63.2 | 6.7 | 252.4 | 3.4 | 21.9 |
| $Py_{I\text{-}Sy}$ (n=17) | | | | | | | | | | | | | | | |
| Min | 0.4 | 15.1 | b.d.l | b.d.l | 3.6 | b.d.l | b.d.l | b.d.l | b.d.l | b.d.l | b.d.l | b.d.l | b.d.l | b.d.l | 0.1 |
| Max | 1017.3 | 948.3 | 73.2 | 41.2 | 9416 | 15.7 | 0.2 | 4.3 | 10.8 | 72.1 | 2.3 | 0.5 | 62.0 | 62.1 | 1.9 |
| Mean | 62.7 | 63.0 | 8.1 | 1.8 | 1131 | 8.3 | 0.0 | 0.9 | 2.5 | 2.3 | 0.4 | 0.1 | 8.6 | 0.2 | 0.3 |
| S.D. | 270.7 | 224.1 | 27.4 | 11.6 | 3505.2 | 3.3 | 0.1 | 1.3 | 3.4 | 31.0 | 0.7 | 0.2 | 18.7 | 17.2 | — |
| $Py_{I\text{-}2}$(n=4) | | | | | | | | | | | | | | | |
| Min | 19.4 | 11.0 | 9.9 | b.d.l | 596 | b.d.l | b.d.l | 0.1 | 1.0 | b.d.l | 0.0 | b.d.l | 9.6 | b.d.l | 0.0 |
| Max | 24.3 | 181.1 | 31.2 | 3.7 | 3692 | b.d.l | 119.8 | 7.6 | 18.1 | 0.7 | 2.4 | 6.1 | 76.1 | 0.5 | 4.2 |
| Mean | 21.7 | 44.8 | 16.2 | 2.7 | 2183 | b.d.l | — | 1.0 | 4.8 | 0.5 | 0.4 | 1.0 | 27.7 | 0.2 | 0.4 |
| S.D. | 2.76 | 76.78 | 11.33 | 1.24 | 1452.58 | — | — | 0.32 | 8.59 | 0.24 | 1.10 | 4.20 | 31.68 | 0.25 | 2.06 |

This is the peer-reviewed, final accepted version for American Mineralogist, published by the Mineralogical Society of America.
The published version is subject to change. Cite as Authors (Year) Title. American Mineralogist, in press.
DOI: https://doi.org/10.2138/am-2020-7508. http://www.minsocam.org/

| | | | | | | | | | | | | | | | |
|---|---|---|---|---|---|---|---|---|---|---|---|---|---|---|---|
| $Py_{II-1}$ (n=14) | | | | | | | | | | | | | | | |
| Min | 6.2 | 47.1 | 7.6 | 2.9 | 3258 | 4.8 | b.d.l | 15.7 | 12.1 | b.d.l | 1.0 | 0.1 | 90.0 | 0.1 | 0.0 |
| Max | 331.8 | 828.0 | 2542.1 | 813.7 | 22838 | 26.5 | 3.8 | 1663.2 | 915.2 | 8.4 | 34.8 | 11.4 | 11205 | 28.3 | 0.5 |
| Mean | 61.2 | 189.3 | 558.0 | 63.4 | 11325 | 8.9 | 0.9 | 58.0 | 241.7 | 2.6 | 4.1 | 2.1 | 1060.5 | 4.1 | 0.1 |
| S.D. | 99.9 | 208.3 | 587.6 | 226.9 | 5076.6 | 6.8 | 1.2 | 414.7 | 296.5 | 2.2 | 9.7 | 2.8 | 3341.1 | 6.9 | 0.1 |
| $Py_{II-2}$ (n=9) | | | | | | | | | | | | | | | |
| Min | 0.0 | 1.2 | 7.0 | 0.4 | 1965 | 5.7 | b.d.l | 1.5 | 2.1 | b.d.l | 0.4 | b.d.l | 14.0 | b.d.l | 0.0 |
| Max | 987.0 | 1152.3 | 99.4 | 70774.0 | 16968 | 19.6 | 0.5 | 731.8 | 1077.1 | 2.0 | 11.1 | 0.3 | 49622 | 1.1 | 7.4 |
| Mean | 8.0 | 26.6 | 19.5 | 6.8 | 6311.3 | 9.3 | 0.0 | 11.7 | 16.8 | 0.5 | 2.3 | 0.1 | 98.5 | 0.1 | 0.2 |
| S.D. | 326.0 | 376.4 | 30.2 | 23589 | 4839 | 7.6 | 0.3 | 6.9 | 354.8 | 0.7 | 4.6 | 0.1 | 16519 | 0.4 | 2.4 |
| Apy (n=13) | | | | | | | | | | | | | | | |
| Min | 15.6 | 80.2 | 113.1 | 0.5 | 446274 | b.d.l | b.d.l | 4.6 | 60.2 | b.d.l | 110.5 | 0.3 | 206.9 | 7.3 | 8.9 |
| Max | 82.6 | 233.1 | 555.5 | 63.1 | 516615 | 12.4 | 1.7 | 18.6 | 111.9 | 8.3 | 353.3 | 4.3 | 558.4 | 12.9 | 34.9 |
| Mean | 26.1 | 113.9 | 239.1 | 2.5 | 474555 | 9.8 | 0.1 | 11.9 | 73.1 | 1.6 | 268.8 | 1.9 | 347.2 | 9.2 | 22.6 |
| S.D. | 216.3 | 239.4 | 160.8 | 15442 | 235796 | 3.9 | 0.5 | 5.1 | 221.1 | 2.0 | 155.6 | 1.3 | 10527 | 4.7 | 12.8 |

b.d.l = below detection limit, S.D.=standard deviation, — =not suitable for calculation.

# Figure 1

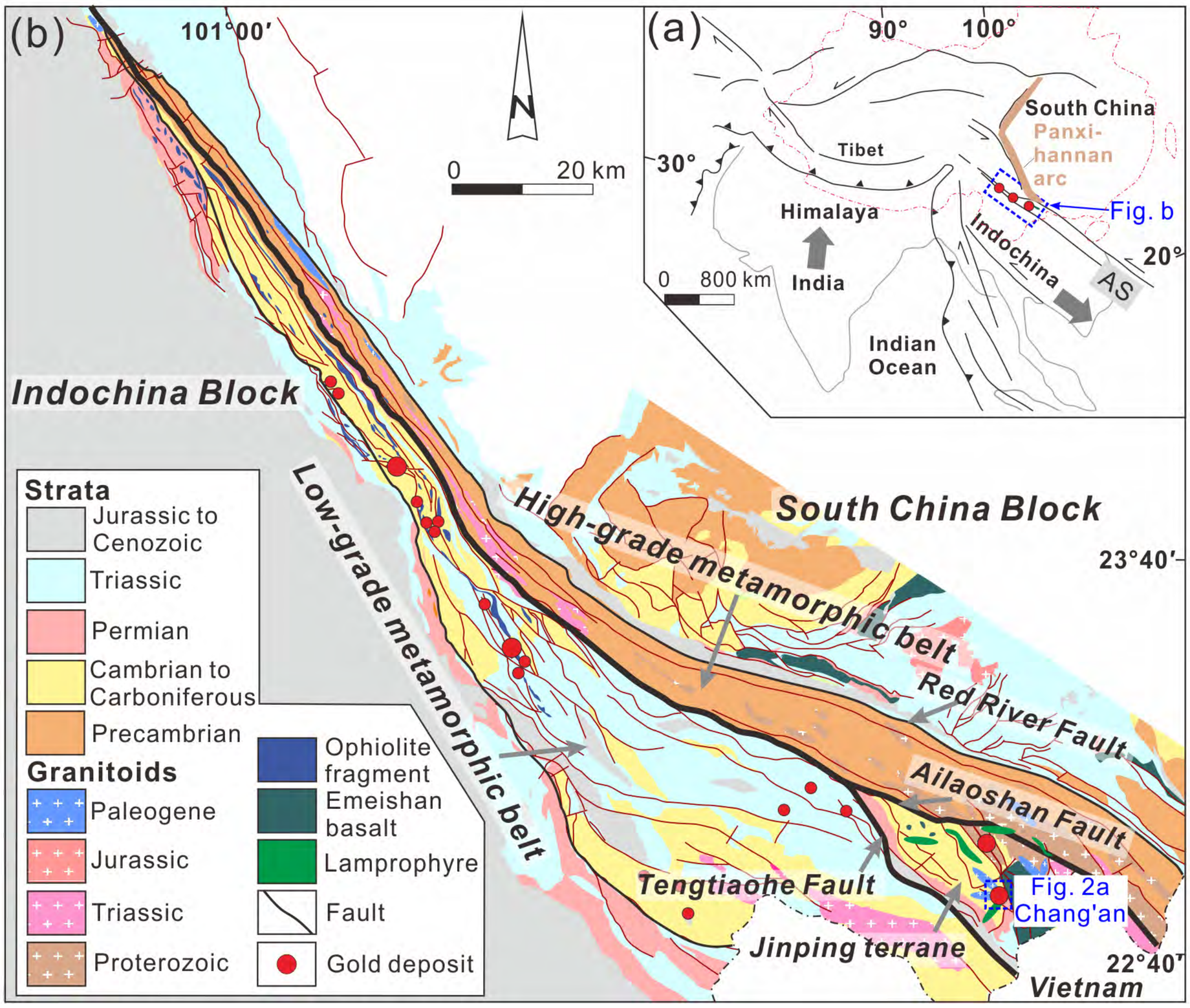

# Figure 2

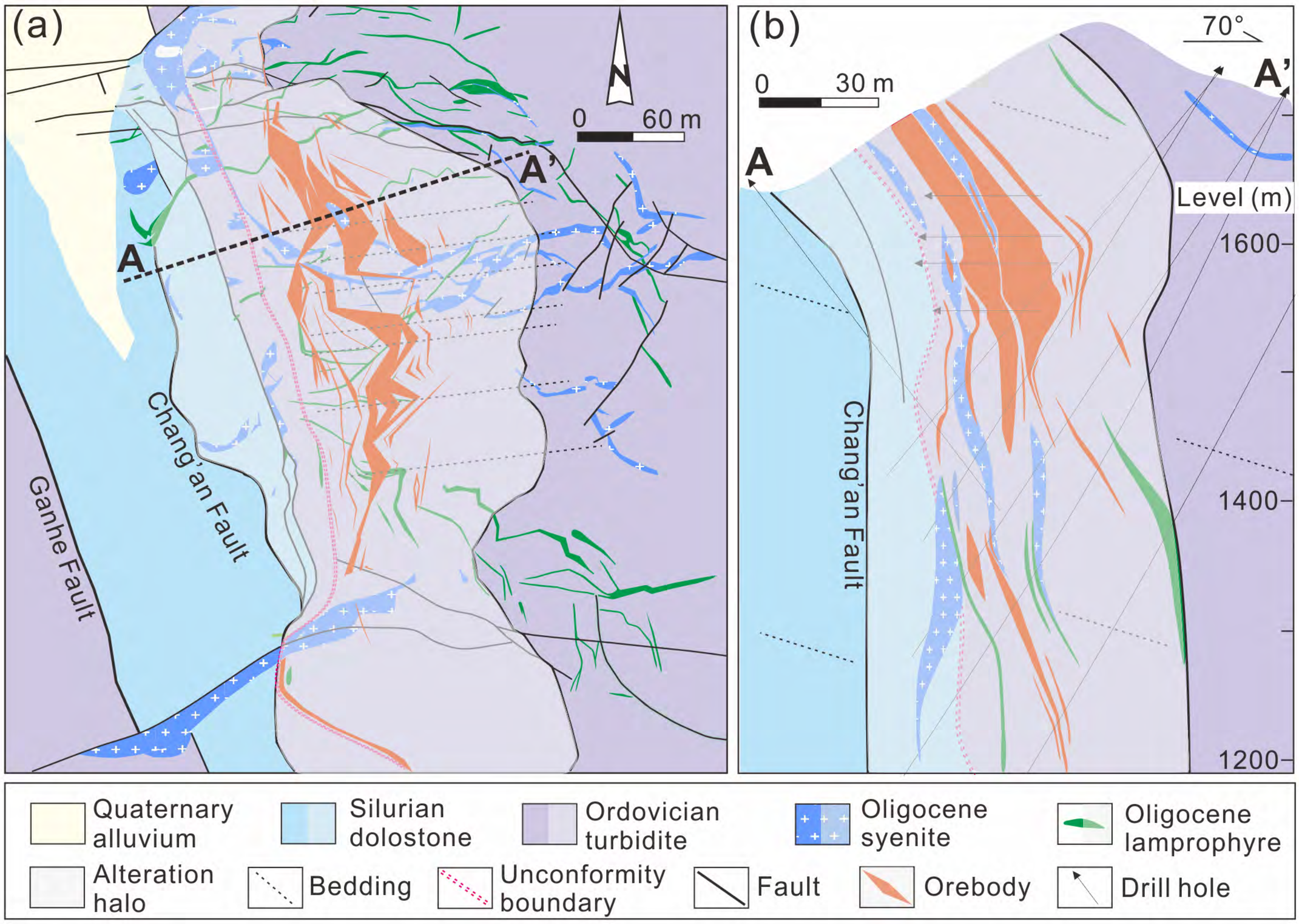

# Figure 3

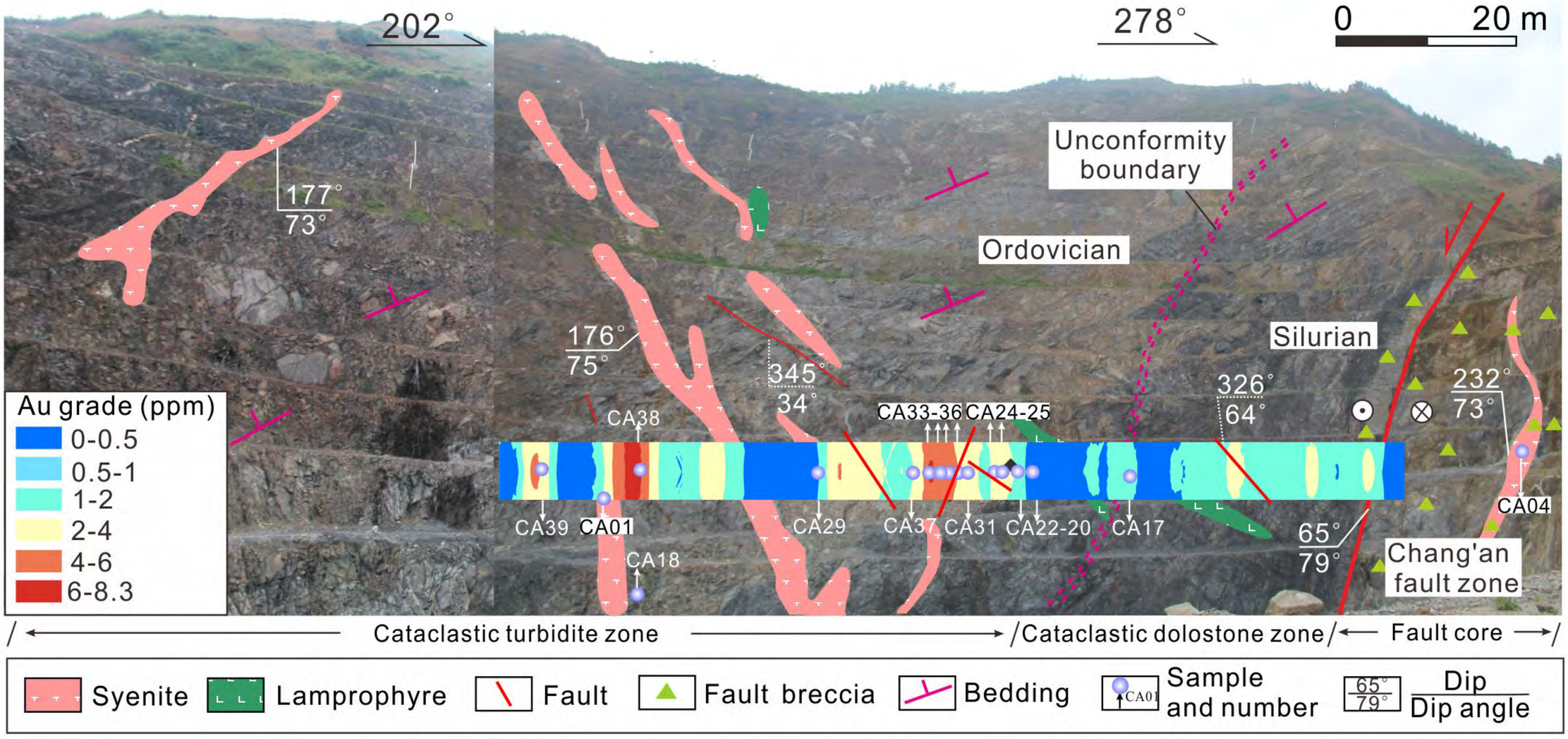

# Figure 4

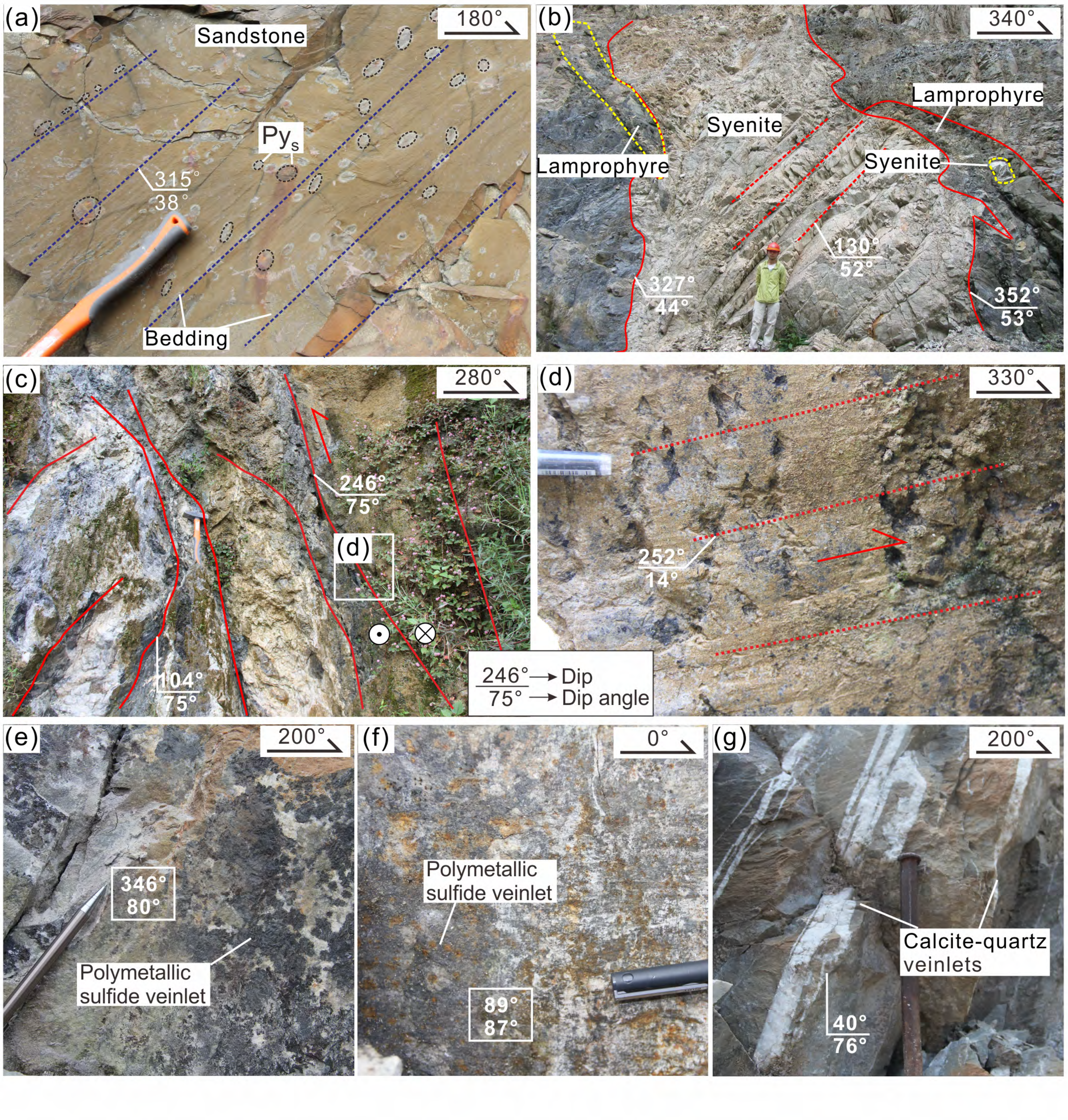

# Figure 5

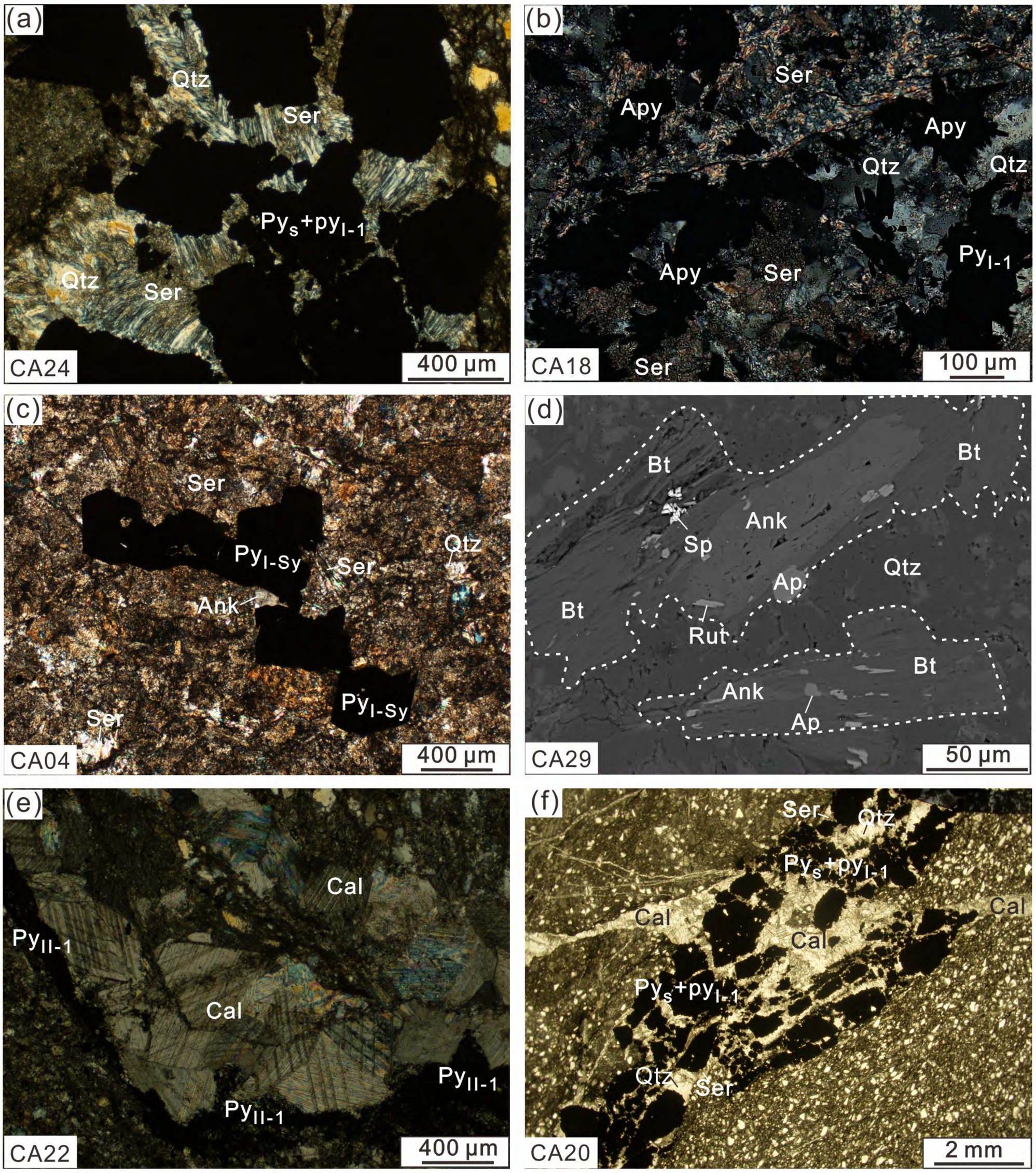

# Figure 6

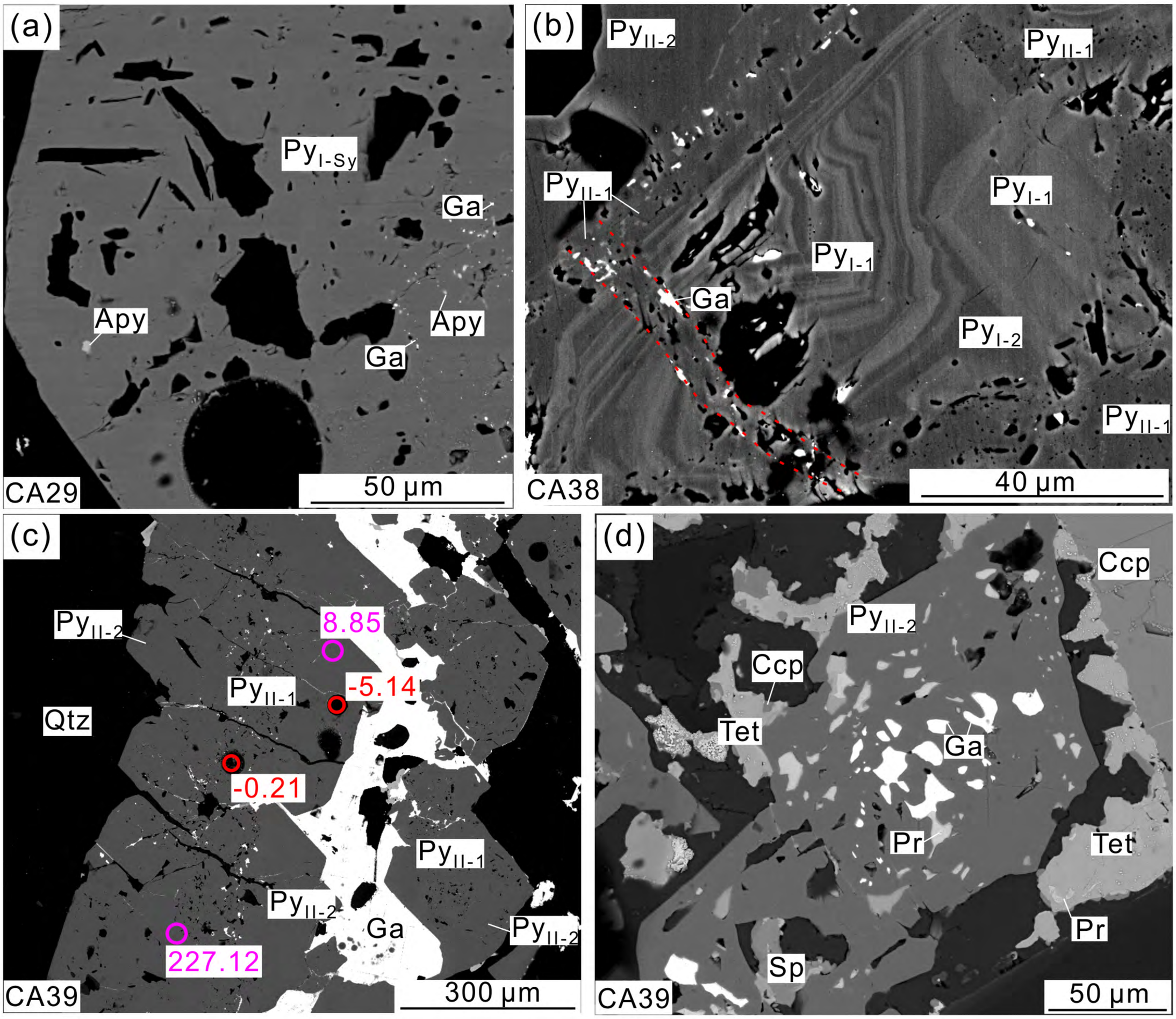

# Figure 7

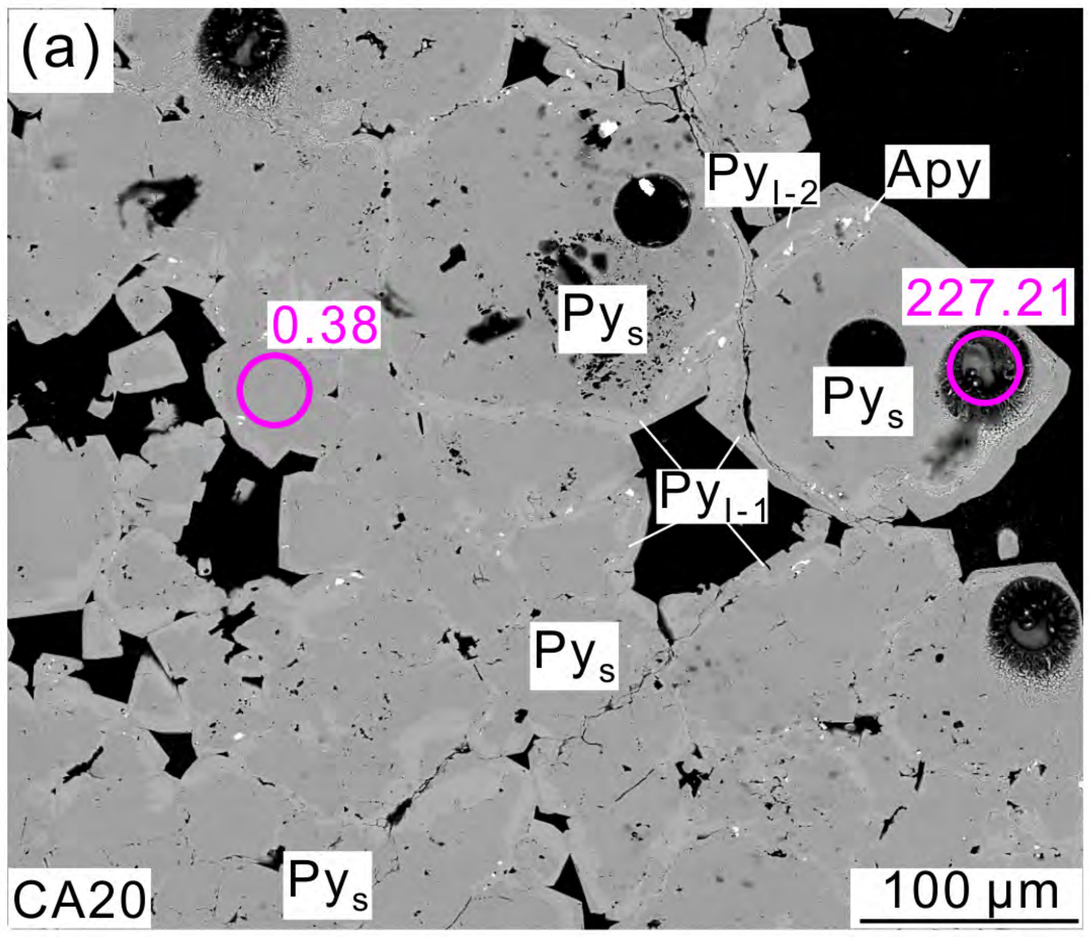


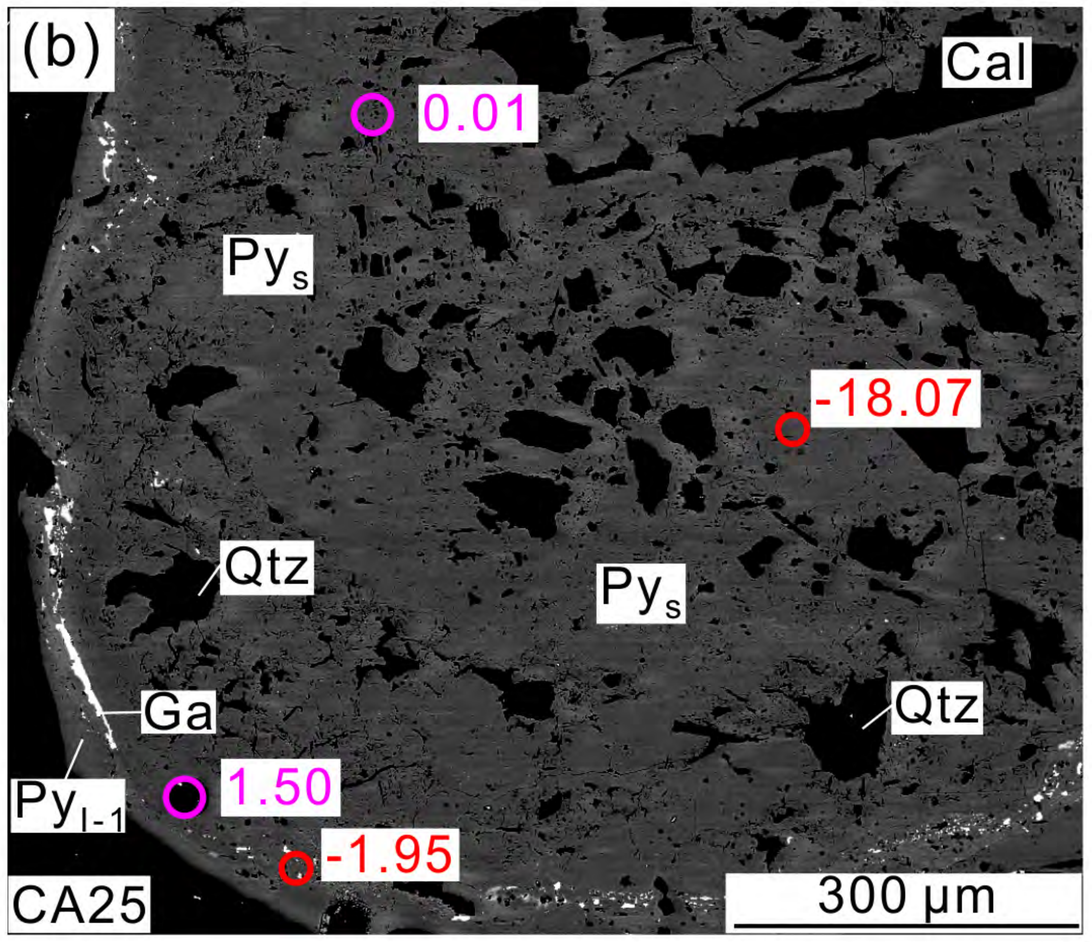


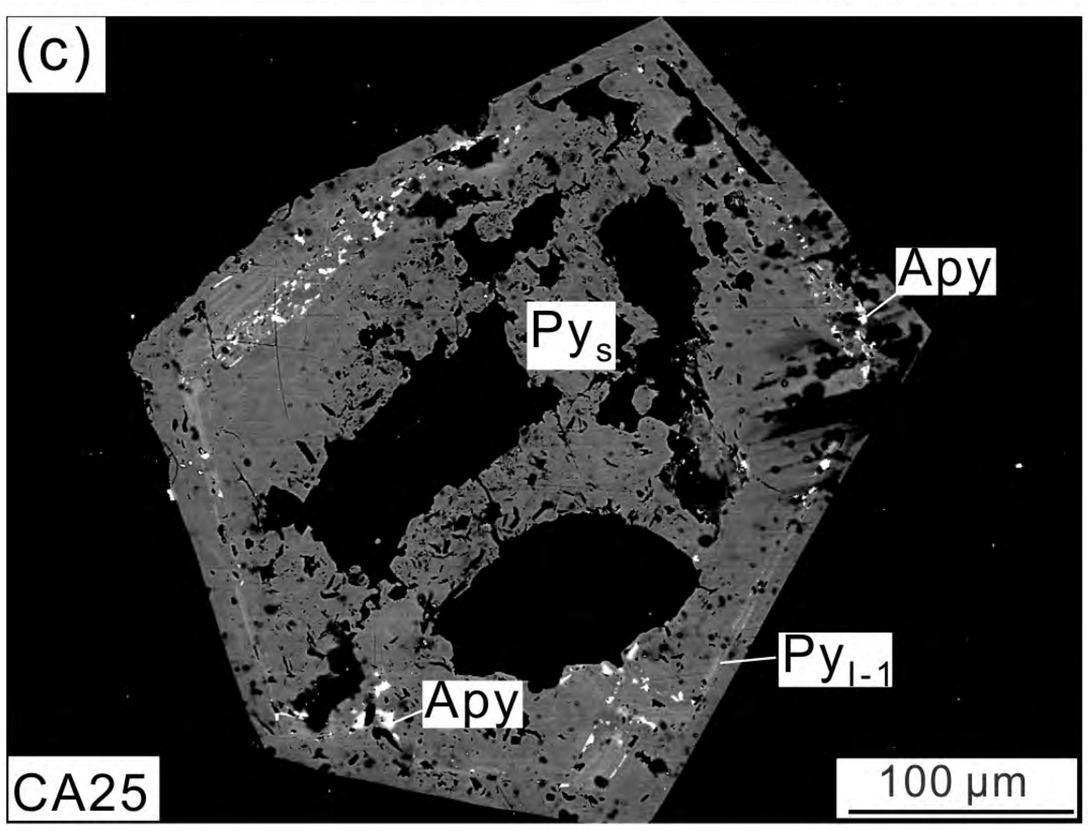


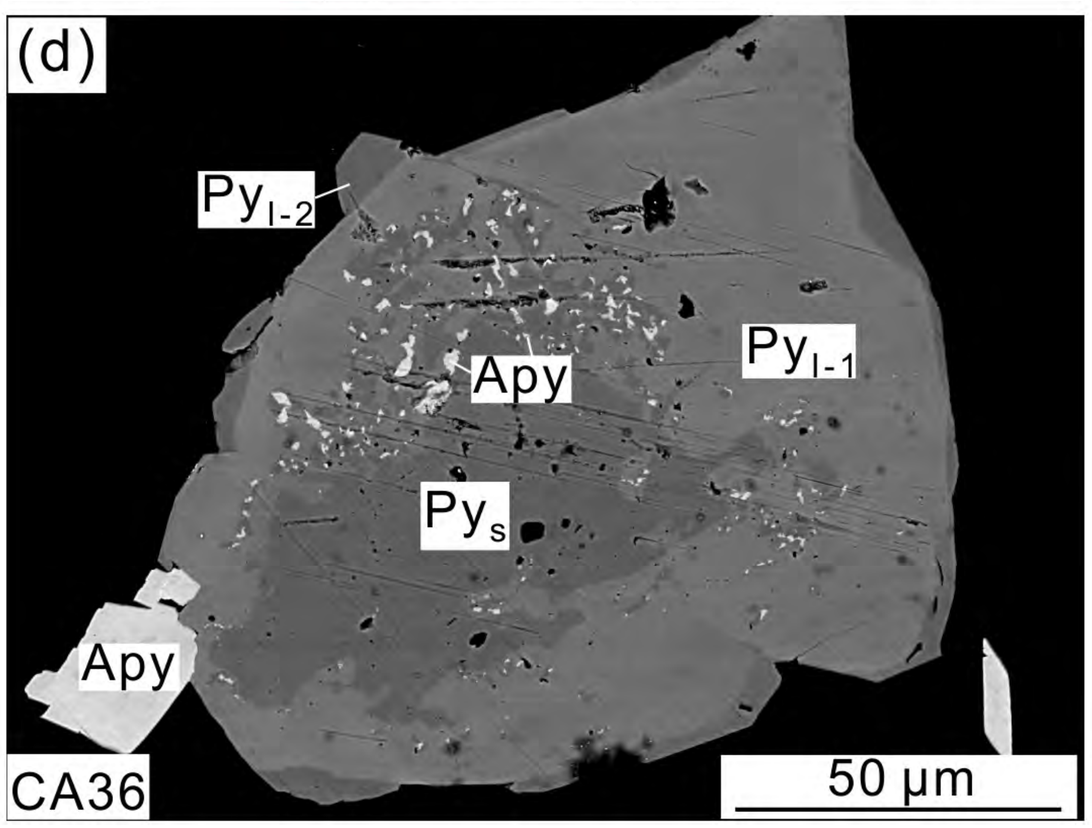

# Figure 8

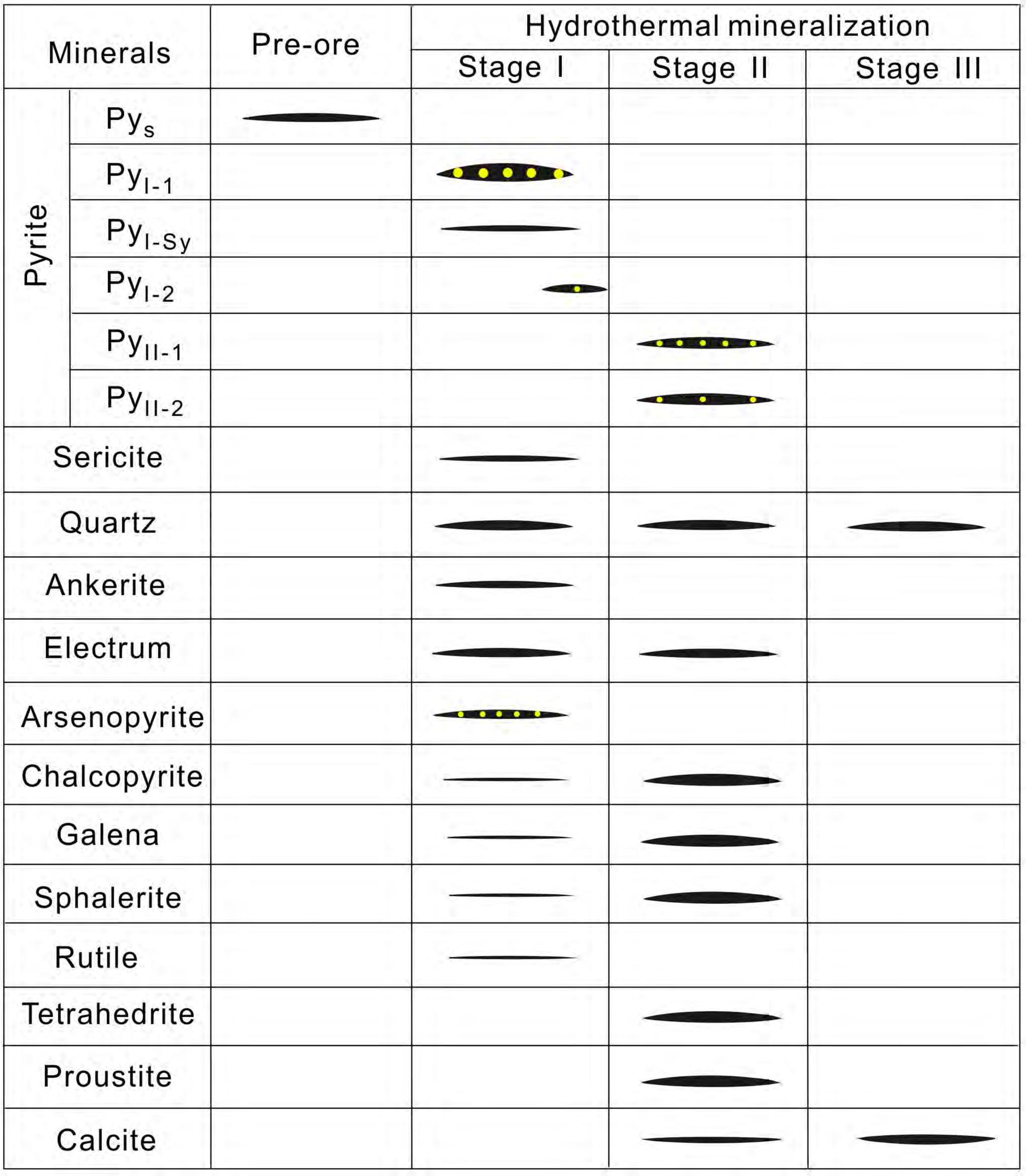

# Figure 9

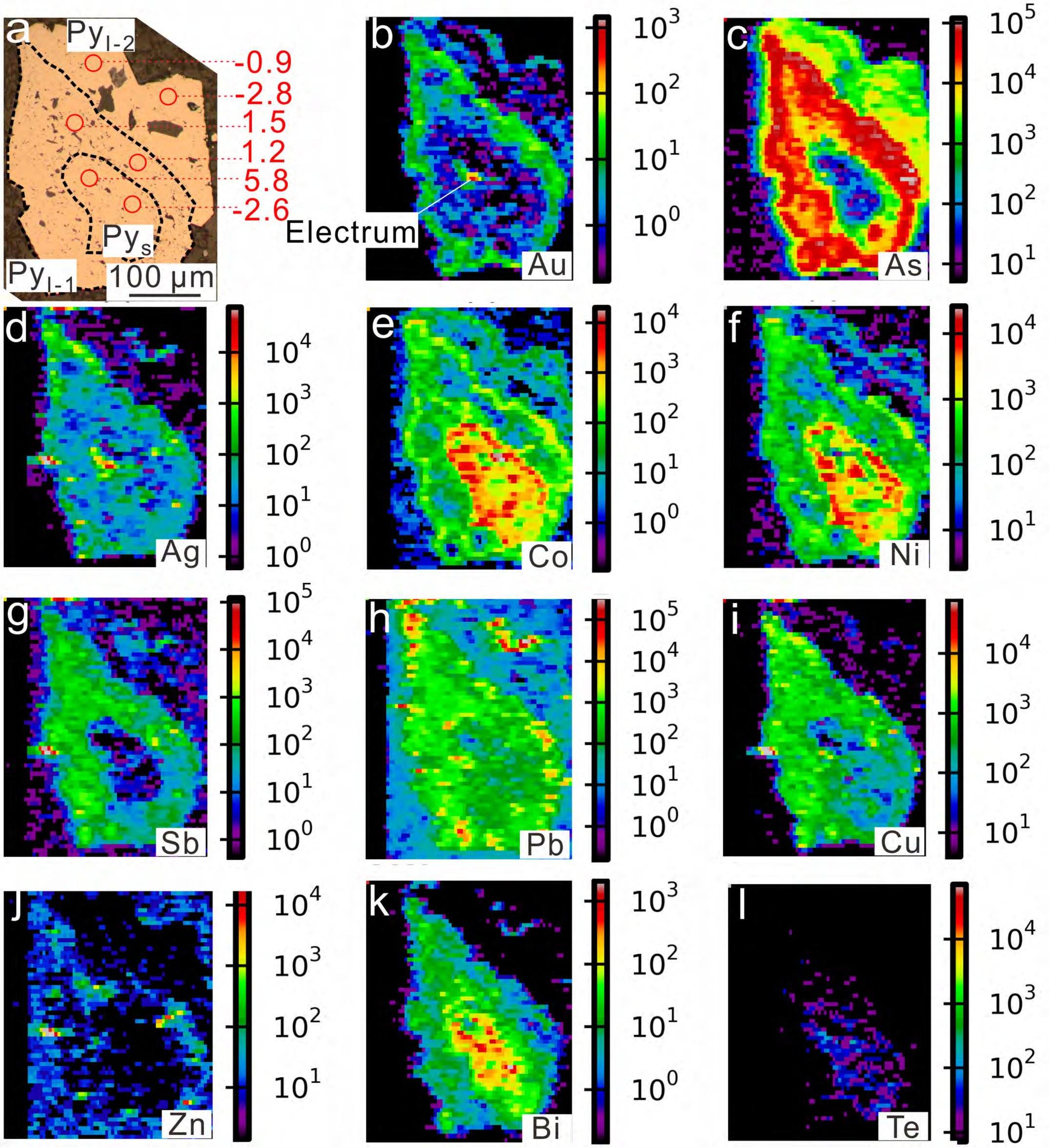

# Figure 10

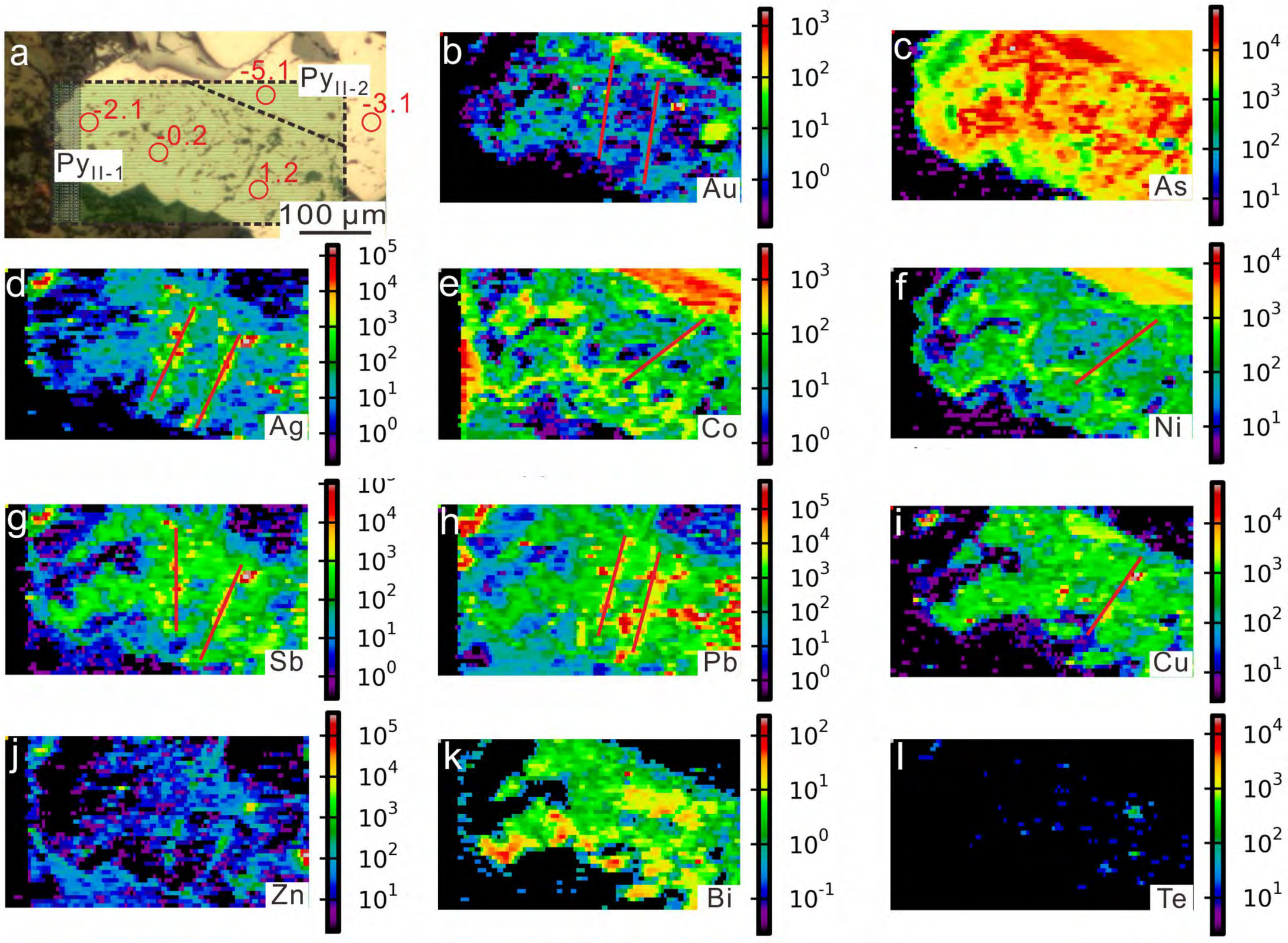

# Figure 11

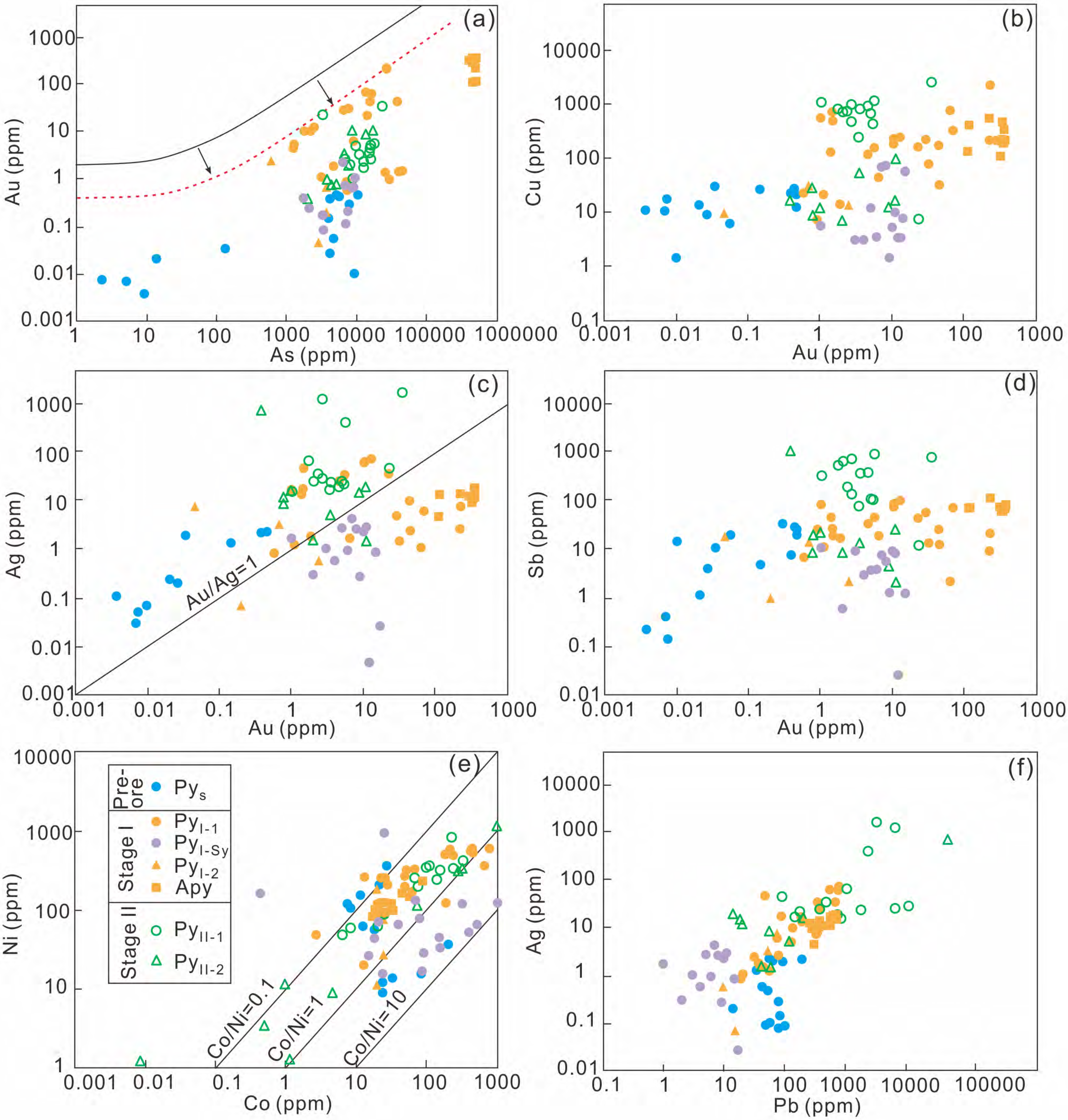

# Figure 12

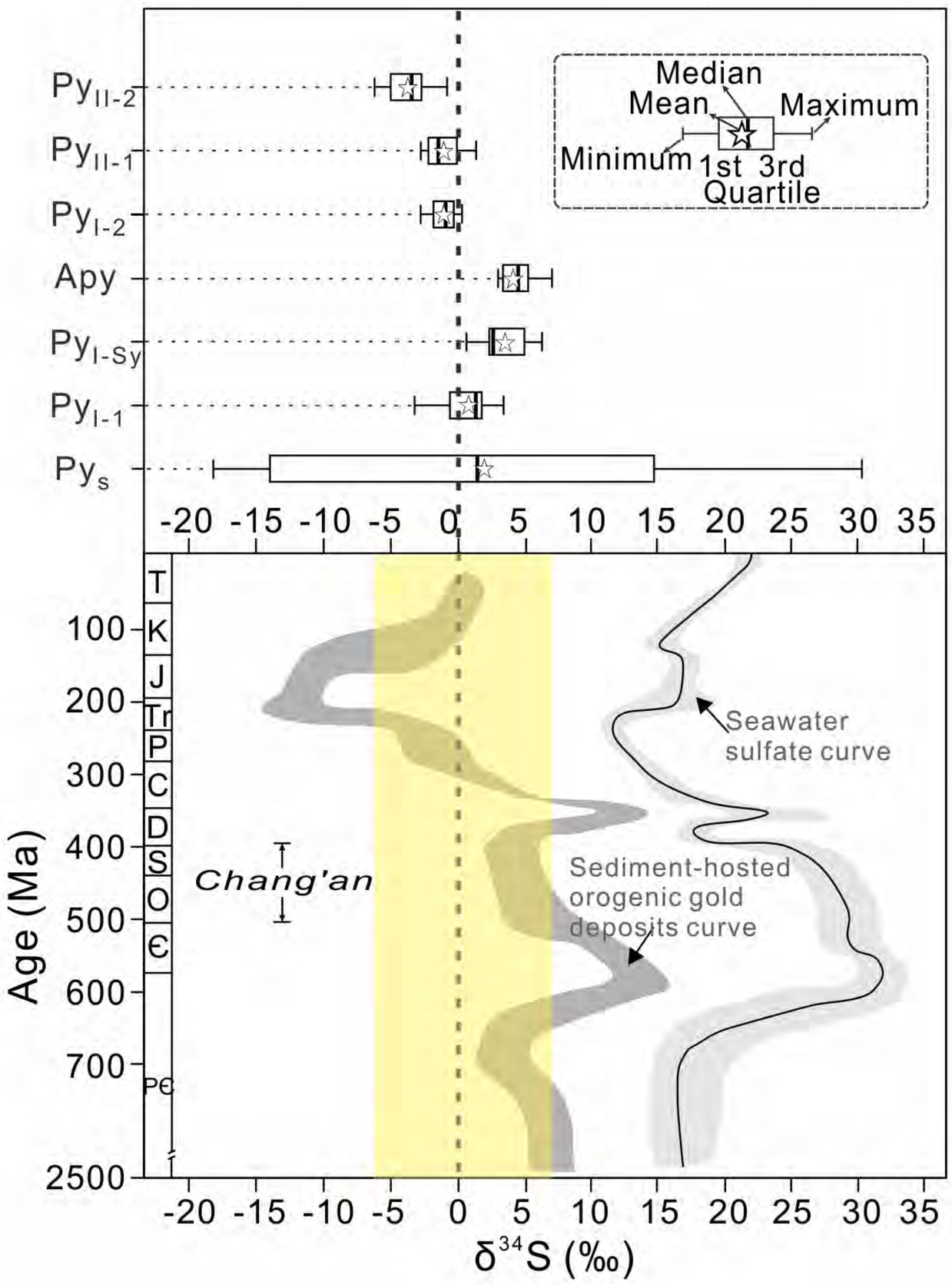

# Figure 13

# Figure 14